

Studies of noctilucent clouds from the stratosphere during the 2024 TRANSAT balloon flight

Peter Dalin¹, Hidehiko Suzuki², Nikolay Pertsev³, Vladimir Perminov³, Linda Megner⁴, Johan Kero¹, Peter Voelger¹, Jonas Hedin⁴, Gerd Baumgarten⁵, Anne Réchou⁶, Denis Efremov⁷

¹ Swedish Institute of Space Physics, Kiruna, Sweden

² School of Science and Technology, Meiji University, Kawasaki, Japan

³ A.M. Obukhov Institute of Atmospheric Physics RAS, Moscow Russia

⁴ Department of Meteorology (MISU), Stockholm University, Stockholm, Sweden

⁵ Leibniz Institute of Atmospheric Physics, Rostock University, Kühlungsborn, Germany

⁶ Lacy Laboratory of Atmosphere and Cyclones, Université de La Réunion, Réunion, France

⁷ Aerospace Laboratory “Stratonautica”, Moscow, Russia

Correspondence to: Peter Dalin (pdalin@irf.se)

Abstract. A transatlantic scientific balloon flight (TRANSAT) was conducted between 22 and 26 June 2024. The TRANSAT balloon, operated by the French Space Agency (CNES), floated in the stratosphere at approximately 40 km altitude between Esrangle (Sweden) and Baffin Island (Canada) for about 3.8 days. The scientific payload comprised nine instruments, including ~~two from the Swedish Institute of Space Physics:~~ an optical imager for noctilucent cloud (NLC) studies **from the Swedish Institute of Space Physics.** ~~and an infrasound instrument for atmospheric infrasound wave investigations.~~ The NLC imager consisted of three identical visible-range optical cameras, one of which operated successfully throughout the entire flight, capturing thousands of NLC images. The TRANSAT balloon campaign was supported by ground-based lidar measurements and spaceborne observations from the Swedish MATS satellite. Here, we describe the technical characteristics of the balloon experiment and present early results. Nearly continuous observations of NLC were obtained during the entire flight. A localized warm region in the mesopause was identified as the cause of temporary NLC disappearance, while complex NLC structures exhibiting different motions were found to probably result from horizontal wind rotation with altitude within the mesopause region.

1 Introduction

Noctilucent clouds (NLC) are the highest clouds in the Earth’s atmosphere, forming in the summer mesopause region between 80 and 90 km altitude at middle and polar latitudes in both hemispheres. They consist of water-ice particles with radii of 30–100 nm that scatter sunlight, making the clouds visible against the twilight sky. NLCs are typically observed from May to September in the Northern Hemisphere and from November to February in the Southern Hemisphere (Gadsden and Schröder, 1989; Liu et al., 2016). When observed from space, these clouds are traditionally called Polar Mesospheric Clouds (PMC) (Thomas, 1984).

38 NLC and PMC are systematically studied using ground-based optical cameras, spectrographs, lidars as well
39 as dedicated spaceborne instruments (e.g., Karlsson and Gumbel, 2005; Dalin et al., 2008; Bailey et al., 2009;
40 Fiedler et al., 2011; DeLand and Thomas, 2015; Tsuda et al., 2022; Wallis et al., 2025). In addition, irregular
41 campaign-based NLC observations are carried out using sounding rockets and aircraft (Zadorozhny et al., 1993;
42 Gumbel and Witt, 2001; Reimuller et al., 2011; Suzuki et al., 2022; Pertsev et al., 2024). Each observational
43 technique has specific advantages and limitations. In particular, ground-based imagers offer high horizontal (~20
44 m) and temporal (~1 s) resolution (Dalin et al., 2010; Baumgarten and Fritts, 2014), and lidars provide high
45 vertical resolution (50–150 m; Baumgarten et al., 2009), but both are restricted by tropospheric weather and
46 limited geographic coverage. Conversely, satellite observations deliver global PMC coverage but suffer from
47 low spatial (~1 km) and temporal (minutes to hours) resolution. Moreover, sun-synchronous satellites introduce
48 large spatial gaps (hundreds of km) between adjacent orbits at mid- and subpolar latitudes (45–60°N) due to a
49 spacecraft orbiting the Earth. Consequently, no single existing technique can fully resolve the microphysical and
50 dynamical processes governing NLC/PMC.

51 Balloon-borne observations from stratospheric altitudes (25–40 km) have a potential for comprehensive
52 studies of NLC on a regular basis. Such observations provide several advantages: independence from
53 tropospheric weather, uninterrupted 24 h coverage, and proximity to the NLC layer (80–85 km), yielding the
54 highest achievable spatial resolution. From this vantage point, both large-scale (up to 2500 km, limited by
55 Earth’s curvature) and small-scale (down to meters) NLC features can be observed. Furthermore, balloon-borne
56 observations at 30–40 km altitude occur above the ozone-rich layer (20–25 km), thereby avoiding light
57 absorption in the Chappuis band (400–650 nm).

58 To date, four balloon-borne experiments have been dedicated to NLC observations from the stratosphere
59 (Miller et al., 2015; Dalin et al., 2019, 2020, 2022; Fritts et al., 2019). These missions have provided unique
60 datasets for studying both large- and small-scale wave dynamics and turbulence within NLC layers. The
61 motivation for the NLC experiment on board the 2024 TRANSAT flight are as follows:

- 62 1. Investigation of temporal-spatial variability of NLC at large- and small-scales in the subpolar and polar
63 mesopause for several days.
- 64 2. Quantification of atmospheric gravity waves at large- and small-scales and turbulent processes, with
65 modeling of propagation pathways and search for wave sources in the underlying atmosphere.
- 66 3. Gaining experience in conducting experiments in the stratosphere for several days.

67 In this study, we present results from a new long-duration balloon experiment aimed at investigating NLC in
68 the polar mesopause. We describe the observation technique and instrumentation as well as early scientific
69 findings. The stratospheric NLC observations were complemented by ground-based lidars and, for the first time,
70 by spaceborne measurements from the Swedish MATS satellite. Additionally, temperature and water vapor data
71 from the Aura/MLS satellite were used to characterize the mesopause environment during the TRANSAT flight,
72 and JAWARA model data were employed to simulate the thermodynamic and wind conditions in support of the
73 NLC observations.

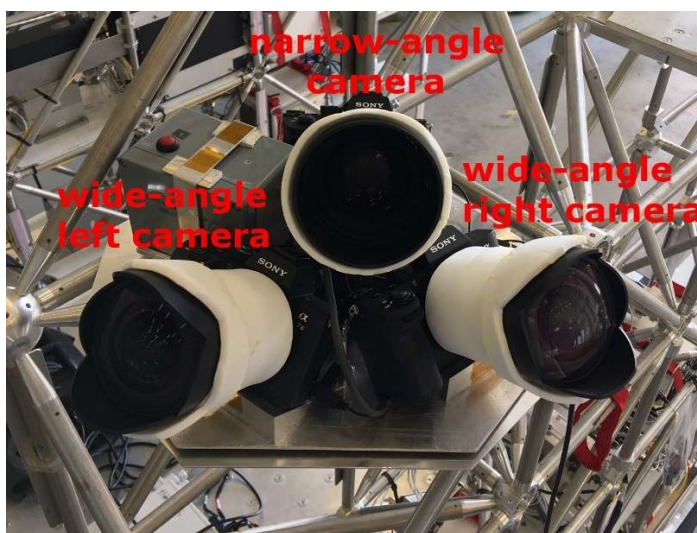
74 **2 Technique and method**

75 **2.1 Technical characteristics of the imager**

76 The Stratospheric Observations of Noctilucent Clouds (SONC) experiment is a balloon-borne scientific
77 mission designed to investigate NLC dynamics across a broad range of spatial scales—from large-scale

78 structures (30–2500 km) to fine-scale features (5 m–30 km)—as well as the microphysical properties of NLC ice
 79 particles.

80 To achieve these objectives, three high-resolution, high-sensitivity Sony $\alpha 7$ Mark III cameras were used.
 81 Each camera has a full-frame 35 mm, 24-megapixel sensor (6000×4000 pixels). Two cameras were equipped
 82 with wide-angle lenses (field of view, FoV, $=105.4^\circ \times 81.8^\circ$), while the third carried a narrow-angle lens
 83 (FoV= $15.0^\circ \times 10.1^\circ$). This configuration, two wide-angle and one narrow-angle camera, provides a horizontal
 84 coverage of about 180° for studying mesospheric NLC structures up to 2500 km across, while simultaneously
 85 enabling spatial resolution as fine as about 5 m when viewing the NLC layer at 83 km from a 40 km altitude and
 86 35° elevation angle. Note that such simultaneous access to both large and small scales is currently unattainable
 87 from either ground-based or satellite platforms. The three cameras formed the SONC imager, illustrated in Fig.
 88 1. Each camera stored data on two 1 TB SD cards. Given the expected 4–5 day duration of the transatlantic flight
 89 and the storage limits, an image acquisition cadence of 50 s was chosen. This temporal resolution enables
 90 tracking the evolution of small-scale wave activity within the NLC layer as well as monitoring large-scale cloud
 91 dynamics. The optical axes of the two wide-angle cameras were inclined at 36° to the horizontal plane in order to
 92 minimize light contamination from bright tropospheric scattering and from above coming from a big white
 93 balloon envelope (~ 70 m in diameter). The narrow-angle camera was tilted at 35° to the horizontal plane to
 94 resolve fine-scale structures of NLC.



95
 96 **Figure 1: The SONC imager consists of three Sony $\alpha 7$ Mark III cameras and the electronic control unit**
 97 **(gray box with red button). Two cameras are equipped with wide-angle lenses, and one with a narrow-**
 98 **angle lens positioned between them. The instrument was used to observe noctilucent clouds during the**
 99 **TRANSAT transatlantic balloon flight (22–26 June 2024).**

100
 101 Sony $\alpha 7$ Mark III camera has a standard Micro USB terminal for power supplying, battery charging and USB
 102 communications, into which an external trigger can be connected to activate the shutter button. For this purpose,
 103 we have developed an external trigger (gray box shown in Fig. 1) that simultaneously transmits the trigger signal
 104 to all three NLC cameras at a certain cadence time (50 s in this experiment). Thus, automatic shooting is carried
 105 out by the three cameras throughout the balloon flight. In addition, this external device distributes power to all
 106 three cameras from an external power supply (a chemical battery on the gondola).

107 Automatic exposure bracketing was applied, capturing 5 images sequentially with exposure times varying
108 between 1/1600 s and 1.6 s. This approach accommodated a wide dynamic range of NLC brightness under
109 variable atmospheric background illumination conditions. One wide-angle camera (left in Fig. 1) operated
110 flawlessly throughout the 3.8-day flight, producing a total of about 40,000 images. The other wide-angle and the
111 narrow-angle cameras functioned for the first 13 h and 12 h, respectively, before ceasing operation for unknown
112 reasons. The imager survived the gondola landing on the ice of Baffin Island without damage. Post-flight tests of
113 all the cameras and electronics confirmed full functionality of the SONC imager and no performance
114 degradation. It should be noted that all three cameras had already been in the stratosphere for about 13 hours at
115 low temperatures of -30°C and were functioning normally (Dalin et al., 2022). Taking into account the previous
116 positive balloon-borne experiment, it was decided to use all three cameras for the long-duration TRANSAT
117 flight in the stratosphere. Also note that SONY $\alpha 7$ Mark III cameras are commercial cameras that are not
118 designed for a flight in the stratosphere in 24/7 sunlight, at low temperatures and low thermal conductivity due to
119 rarefied air. The electronics inside the two cameras could freeze or overheat. This is the most likely reason for
120 the failure of these two cameras after 12 h of the flight.

121

122 **2.2 Technical characteristics of the TRANSAT balloon flight**

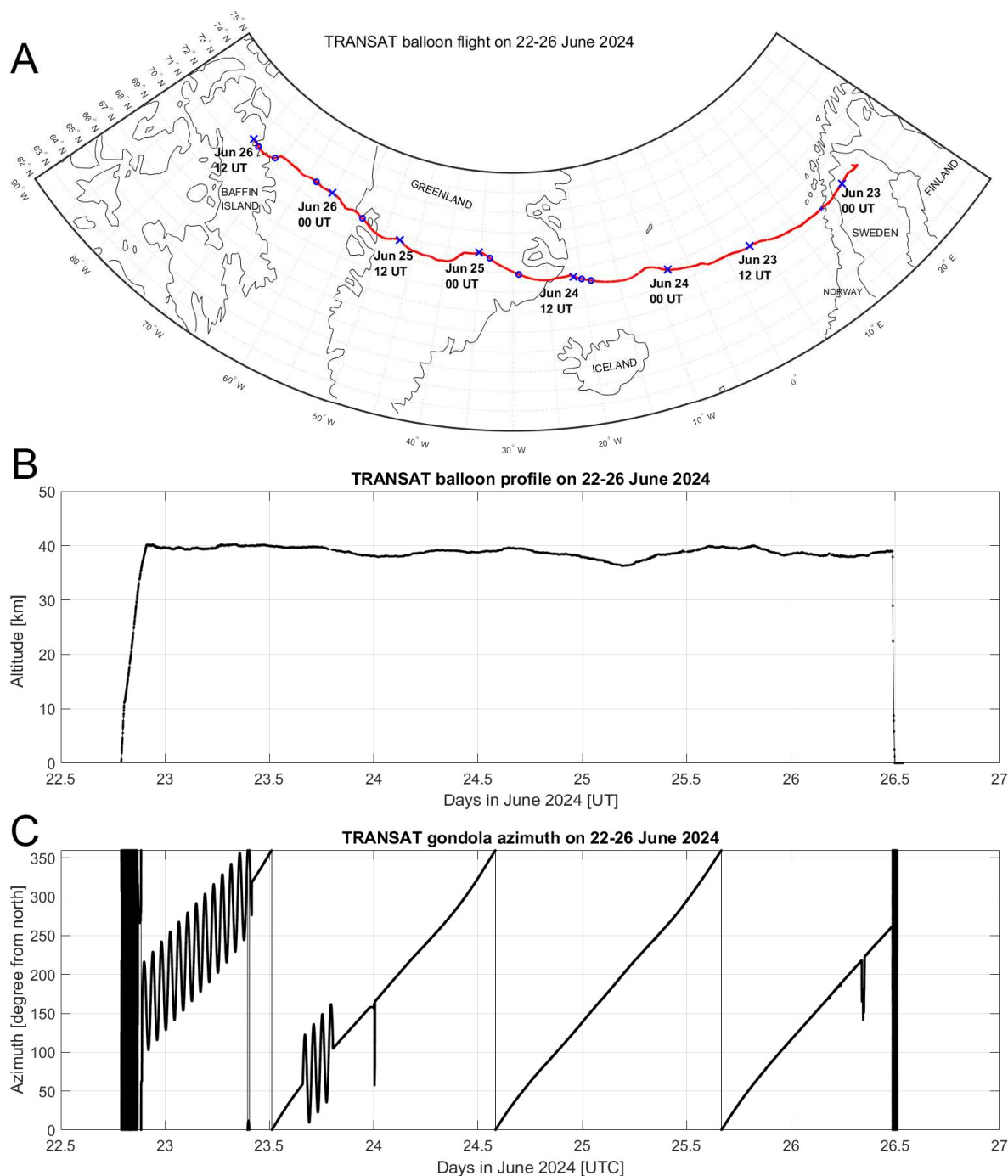
123 The TRANSAT mission is a long-duration stratospheric balloon flight organized and operated by the French
124 Space Agency (CNES) (https://stratocat.com.ar/fichas-e/2024/KRN_20240622-htm) for multidisciplinary
125 atmospheric and cosmic research. The gondola, named Carmen, had a total mass of about 900 kg and carried
126 nine scientific instruments. Two of these were from Sweden: the SONC imager and an infrasound instrument
127 dedicated to studies of infrasound atmospheric waves and their sources. The infrasound experiment and its
128 scientific results will be described in a separate paper.

129 The Carmen gondola utilized a three-axis motorized gimbal stabilized platform, providing an elevation-angle
130 stability of 0.15° , an absolute azimuth pointing accuracy of 1° and a stability of ± 10 arcmin around it. Because
131 stratospheric balloons rotate continuously, such stabilization was critical to avoid image smearing and to
132 maintain consistent NLC monitoring at fine and large scales.

133 As the transatlantic flight took place under solstice conditions with continuous solar illumination, scientific
134 instruments were mounted behind a solar shield to prevent overheating and stray-light interference. To ensure
135 continuous shading, the gondola was slowly rotated to keep the solar shield facing the Sun throughout the flight.
136 Due to different scientific experiments onboard requiring different pointing directions, sometimes the anti-sun
137 direction was not observed, but the oscillations around the leading azimuth of the gondola remained under
138 control (see Fig. 1c). When the Sun illuminated the camera lens or strong solar reflections were present, such
139 images were removed from the image analysis as overexposed. The number of the overexposed removed image
140 accounted for about 2% of the total number of images analyzed.

141 The TRANSAT balloon was launched from Esrange, northern Sweden (67.89°N , 21.08°E) at 18:57 UTC
142 (20:57 LT) on 22 June 2024 and landed on Baffin Island, northern Canada, at 12:14 UTC (08:14 LT) on 26 June
143 2024. The total flight time was about 90 h (3.8 days), with an average horizontal speed of about 11 m s^{-1} . The
144 horizontal trajectory and altitude profiles of the TRANSAT mission are shown in Fig. 2.

145



146
 147 **Figure 2: (A) Horizontal trajectory (the red line) of the TRANSAT balloon mission between 22 and 26**
 148 **June 2024. The blue crosses mark the balloon’s position every 12 h. The blue circles show the balloon’s**
 149 **positions when no NLC were observed, see Section 4.1. (B) Altitude profile of the TRANSAT flight. (C)**
 150 **Azimuth of the optical axis of the left camera of the SONC imager due to the TRANSAT gondola rotation**
 151 **in the anti-sun direction for most of the flight.**

152

153 2.3 Image processing

154 Prior to launch, all three Sony cameras underwent geometrical calibration on the ground using night-sky
 155 images containing reference stars. A second-order polynomial camera model was fitted by comparing theoretical
 156 and measured horizontal coordinates for over 200 identified reference stars. Six free coefficients describing focal

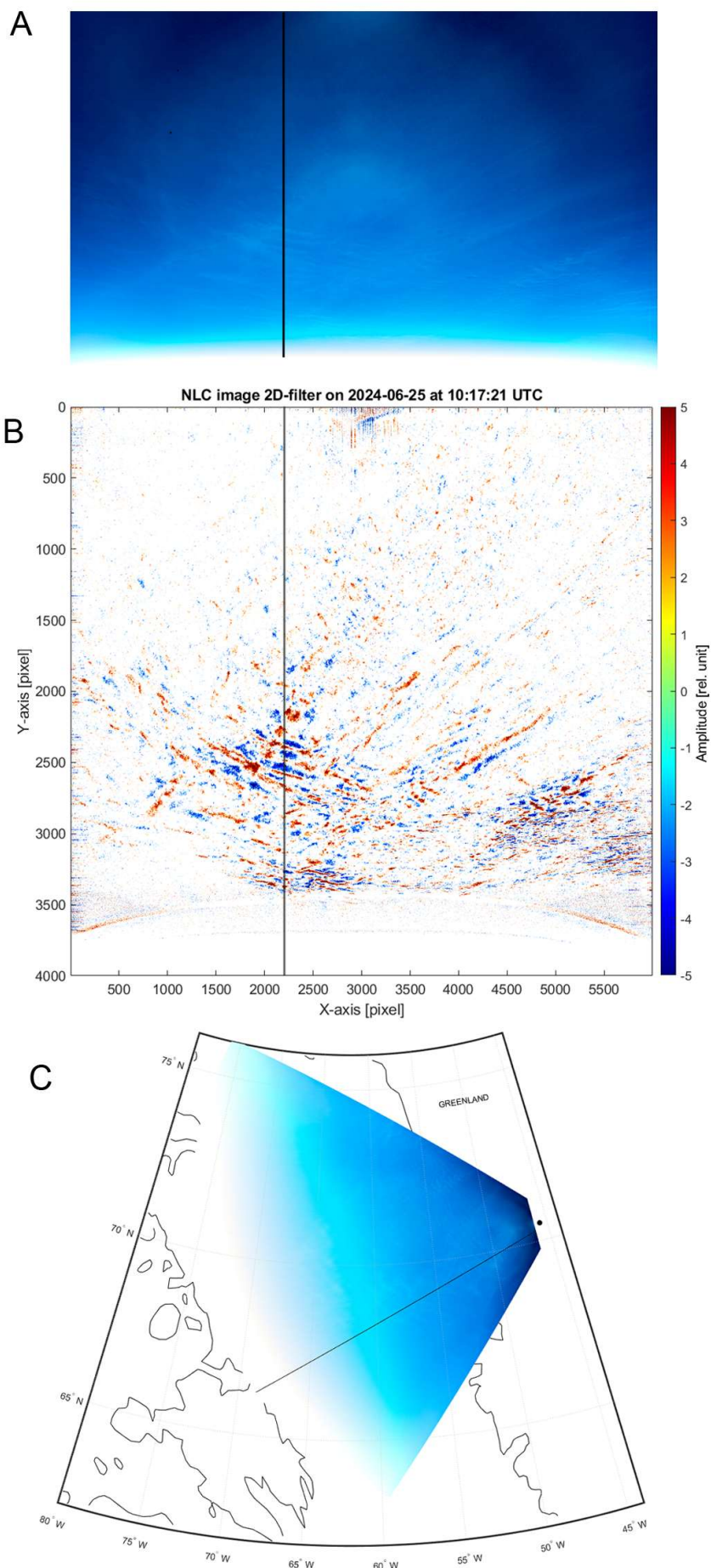
157 length, image orientation, and optical distortion were determined. These coefficients were used to compute
158 relative horizontal coordinates (elevation and azimuth angles relative to the center of the image) for every pixel
159 of each camera.

160 Given the known position and orientation of the SONC imager within the gondola reference frame, provided
161 by CNES, the absolute horizontal coordinates of all pixels were computed. Subsequently, a georeferencing
162 procedure projected each pixel onto the Earth's surface, assuming a mean NLC altitude of 83 km. Details of the
163 calibration, georeferencing, and error analysis are available in Dalin et al. (2015).

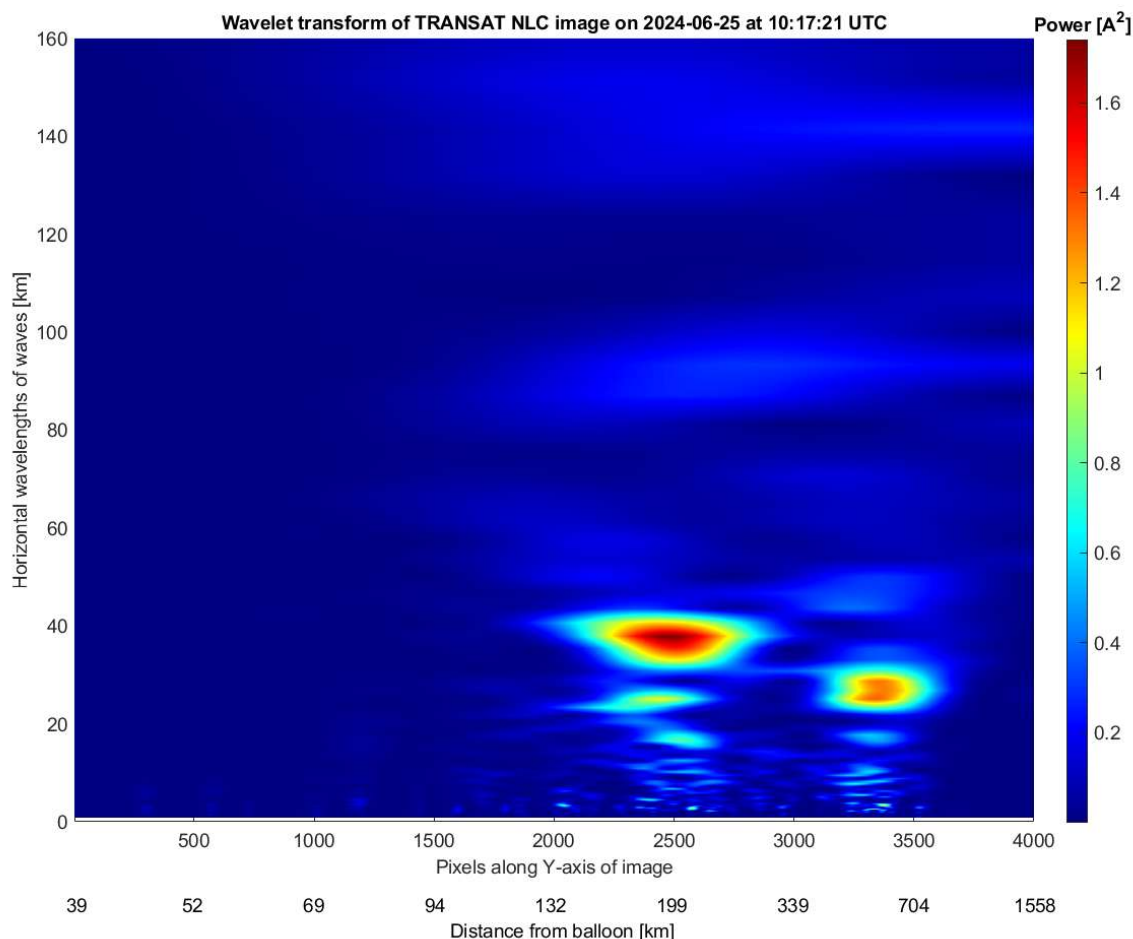
164 NLC identification was performed using both manual and automatic approaches. In the manual procedure,
165 about 6200 images, suitable for scientific analysis, from the left camera (Fig. 1) were carefully examined to mark
166 NLC presence or absence. A separate text file was created that indicates the cloud-free times during the
167 TRANSAT flight. The number of images is 6200 because almost every image in a series of 5 images, taken in
168 bracketing mode, was analyzed. A video sequence was then assembled to verify temporal continuity. This video,
169 containing all images with synchronized flight parameters, timestamps and balloon coordinates, is available at
170 the Harvard Dataverse repository (<https://doi.org/10.7910/DVN/1PHRZU>).

171 Automatic image processing involved several steps: (1) Background subtraction: a second-order polynomial
172 fit was used to estimate the sky background along each vertical column of pixels, which was then subtracted to
173 yield a residual brightness of each pixel. (2) Two-dimensional digital filtering: applied to a residual brightness to
174 extract gravity-wave-like patterns on image (see Fig. 3b). To do this, we use zero-phase digital filtering by
175 processing the residual brightness in forward and reverse directions along every vertical and horizontal line of
176 the analyzed image. After filtering the data in the forward direction, the procedure reverses the filtered sequence
177 and runs it back through the filter that provides a zero-phase distortion. A 4th-order Butterworth bandpass filter
178 with a lower cutoff frequency of 0.0013 Hz and a higher cutoff frequency of 0.2 Hz is applied in this digital
179 filtering procedure. (3) Wavelet analysis: a Morse analytic wavelet transform was applied to selected images to
180 quantify horizontal wavelengths of identified wave patterns. An analyzed image was first projected onto Earth
181 geographical coordinates (in km) prior to wavelet analysis. An example (Fig. 4) shows dominant horizontal
182 wavelengths of about 30 and 40 km, which are frequently observed in NLC (Pautet et al., 2011; Demissie et al.,
183 2014). In the present case, wave analysis was applied to the vertical slice (along the Y-axis) at the constant
184 $X=2200$ pixels of the filtered image shown in Fig. 3b. This example was chosen at random from 6200 images,
185 but which demonstrates the NLC modulation due to gravity waves with the naked eye. Therefore, this analysis
186 technique was applied to this image in order to estimate the horizontal scales of the wave packet in this case.

187 The spatial horizontal resolution of the pixels in the upper part of the projected image (close to the balloon) is
188 about 21 m, of the pixels in the middle of the image is about 96 m, and of the pixels at the bottom of the
189 projected image is about 1.2 km. In accordance with the Nyquist–Shannon sampling theorem, these values allow
190 the study of NLC signals with horizontal scales greater than 42 m, 192 m and 2.4 km, respectively. Thus,
191 medium- and large-scale gravity waves with horizontal wavelengths greater 50 km, small-scale gravity waves of
192 10-50 km, smaller-scale localized waves (billows or ripples) of 3-10 km can be analyzed throughout the image.
193 Also, turbulent structures like vortex rings of 0.5-4 km in diameter can be studied in the upper and middle part of
194 the image (Dalin et al., 2010; Pautet et al., 2011; Baumgarten and Fritts, 2014; Fritts et al., 2017; Fritts et al.,
195 2019).



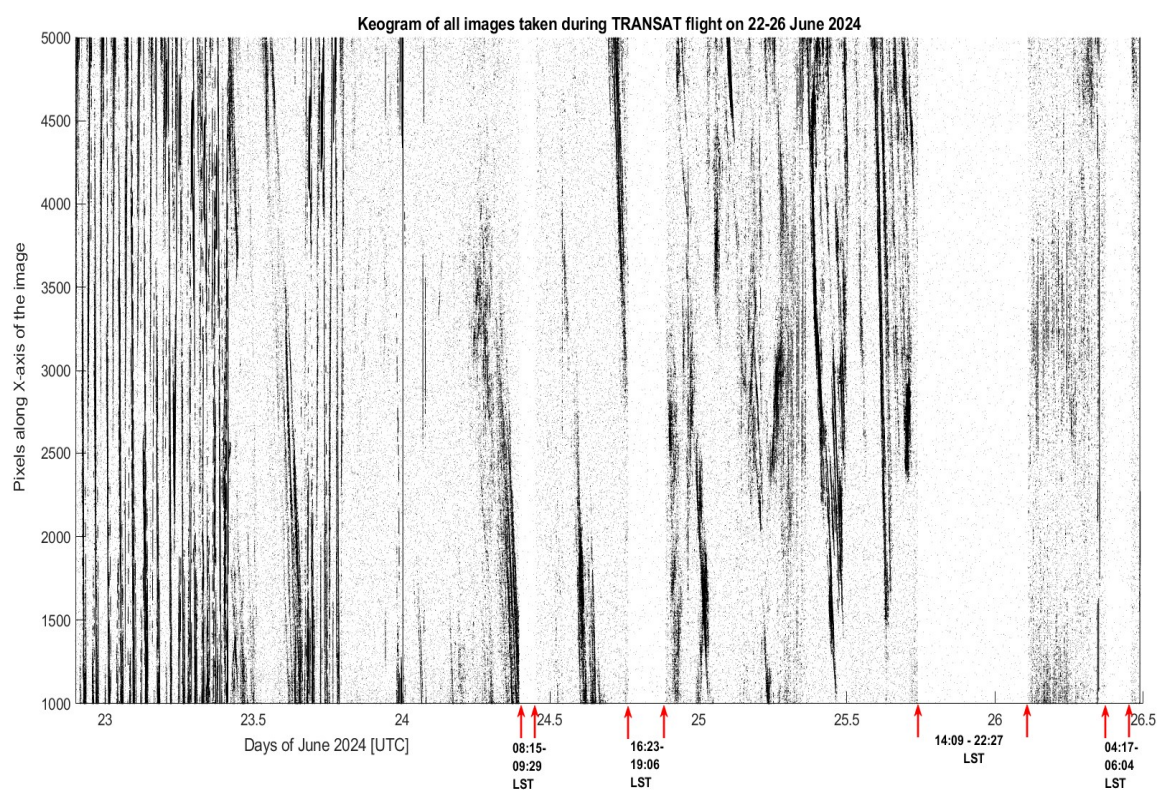
197 **Figure 3: (A) Example of NLC image acquired at 10:17:21 UTC on 25 June 2024 during the TRANSAT**
 198 **balloon flight. (B) Two-dimensional Fourier-filtered version of (A), highlighting residual brightness**
 199 **variations associated with NLC bands seen in the middle and the lower part of the image. (C) Projection**
 200 **of the NLC image shown on panel A onto the Earth's surface. The black dot is the position of the**
 201 **TRANSAT balloon. The black line shown in panels A, B and C shows the vertical slice at X=2200 pixels**
 202 **where wavelet analysis was applied (see the text).**
 203



204 **Figure 4: Example of a wavelet transform for the NLC image obtained at 10:17:21 UTC on 25 June 2024**
 205 **during the TRANSAT flight. Gravity waves having prevailing horizontal scales of about 30 and 40 km are**
 206 **clearly seen as the red color code. Two different scales on the X-axis are present: the upper scale is in**
 207 **pixels along the Y-axis at X=2200 pixels of the image shown in Fig. 3a, the lower scale is the distance from**
 208 **the TRANSAT balloon in km.**
 209

210
 211 4) A keogram representation of a sequence of all analyzed images helps to identify the presence or absence of
 212 NLC as a function of time. A keogram is a slice of an image along a specific axis, and many such slices are put
 213 together as a function of time to produce brightness variations of an observed atmospheric phenomenon over
 214 time. A keogram is commonly used to demonstrate a presence or absence of aurora in all-sky images. In the
 215 present study, based on the manual careful inspection of 6200 images suitable for scientific analysis, we have
 216 selected horizontal pixel lines in the range of 3000-3400 pixels (counting along the Y-axis from the top of the

217 image) at which NLC preferred to appear. These pixels correspond to a distance of about 315-583 km from the
 218 gondola position, when looking along the central line of the image. The image coordinates are present in Fig. 3b.
 219 These pixels were summed to produce an integrated brightness for every column between 3000 and 3400 pixels.
 220 The mean value and its standard deviation (std) were then calculated for the given slice along the X-axis of the
 221 image. We have separately estimated the mean brightness and its standard deviation for each image, thus the
 222 obtained values are independent of time and camera azimuth. Next, a selection rule was applied: brightness
 223 values greater than 1 std of the mean were selected to classify the given slice as NLC present or absent. Then the
 224 keogram was created by putting together slices of about 6200 images (Fig. 5), demonstrating nearly continuous
 225 presence of NLC, that is discussed in detail in Section 4. This automatic keogram procedure fits well with the
 226 manual procedure (described above) in identifying the presence or absence of NLC as a function of time. The
 227 time intervals of the absence of NLC are indicated by red arrows that coincide with the manual and automatic
 228 procedure.



229
 230 **Figure 5: Keogram compiled from about 6200 images during the TRANSAT balloon flight on 22-26 June**
 231 **2024. The red arrows mark four time intervals (white-grey areas) when NLC were absent. Corresponding**
 232 **local solar times (LST) are shown for four time intervals on the x-axis. LST are calculated for the gondola**
 233 **position, but not for the observed NLC. The number of Y-pixels is equal to 401 for which the keogram was**
 234 **constructed.**

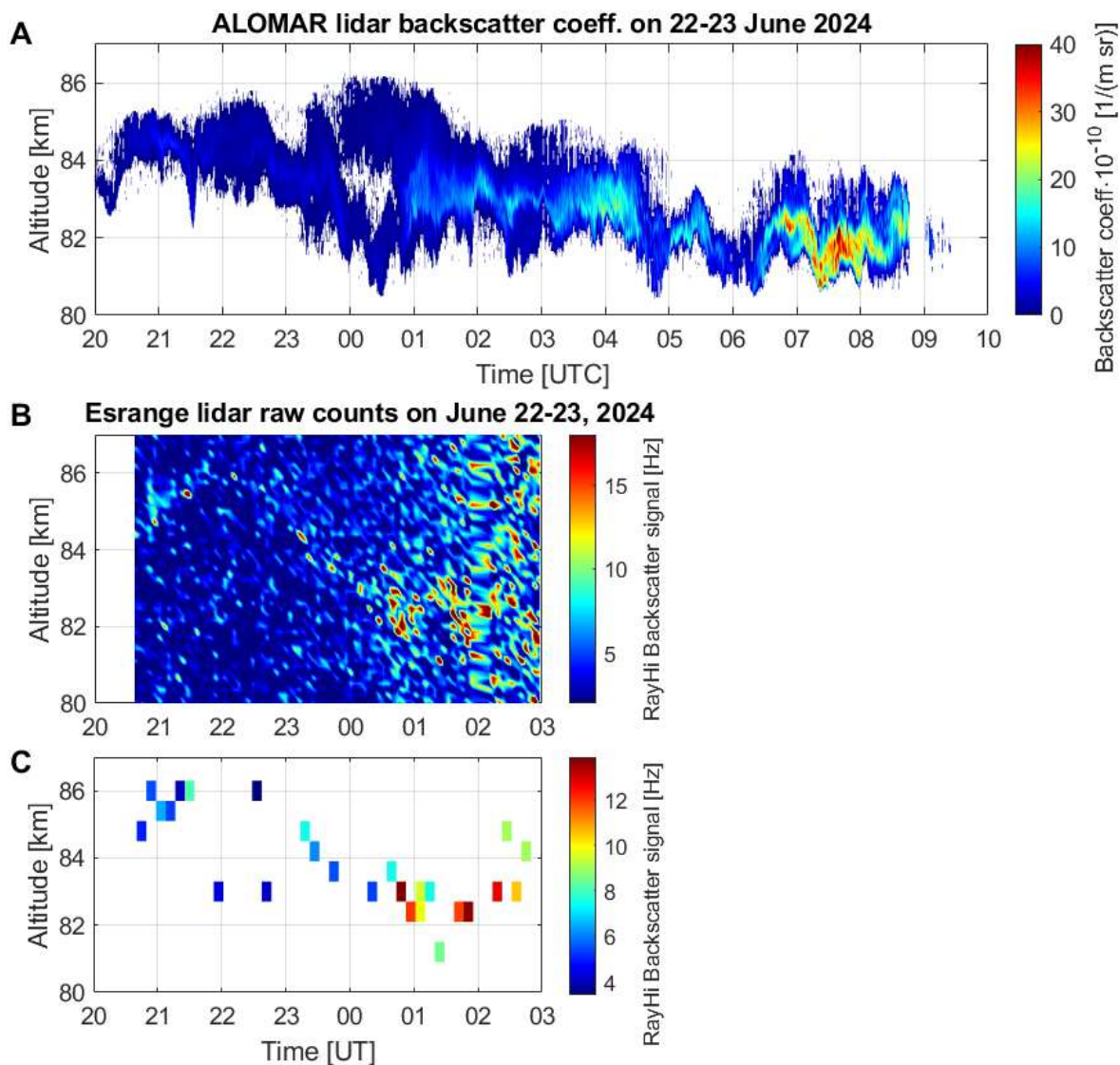
235 236 3 Ground-based and space complementary measurements

237 3.1 Lidar measurements

238 During the initial phase of the TRANSAT balloon flight, complementary lidar measurements were
 239 performed at Esrange (67.8°N, 21.1°E, Sweden) and Andøya (69.3°N, 16.0°E, Norway), with the aim to provide

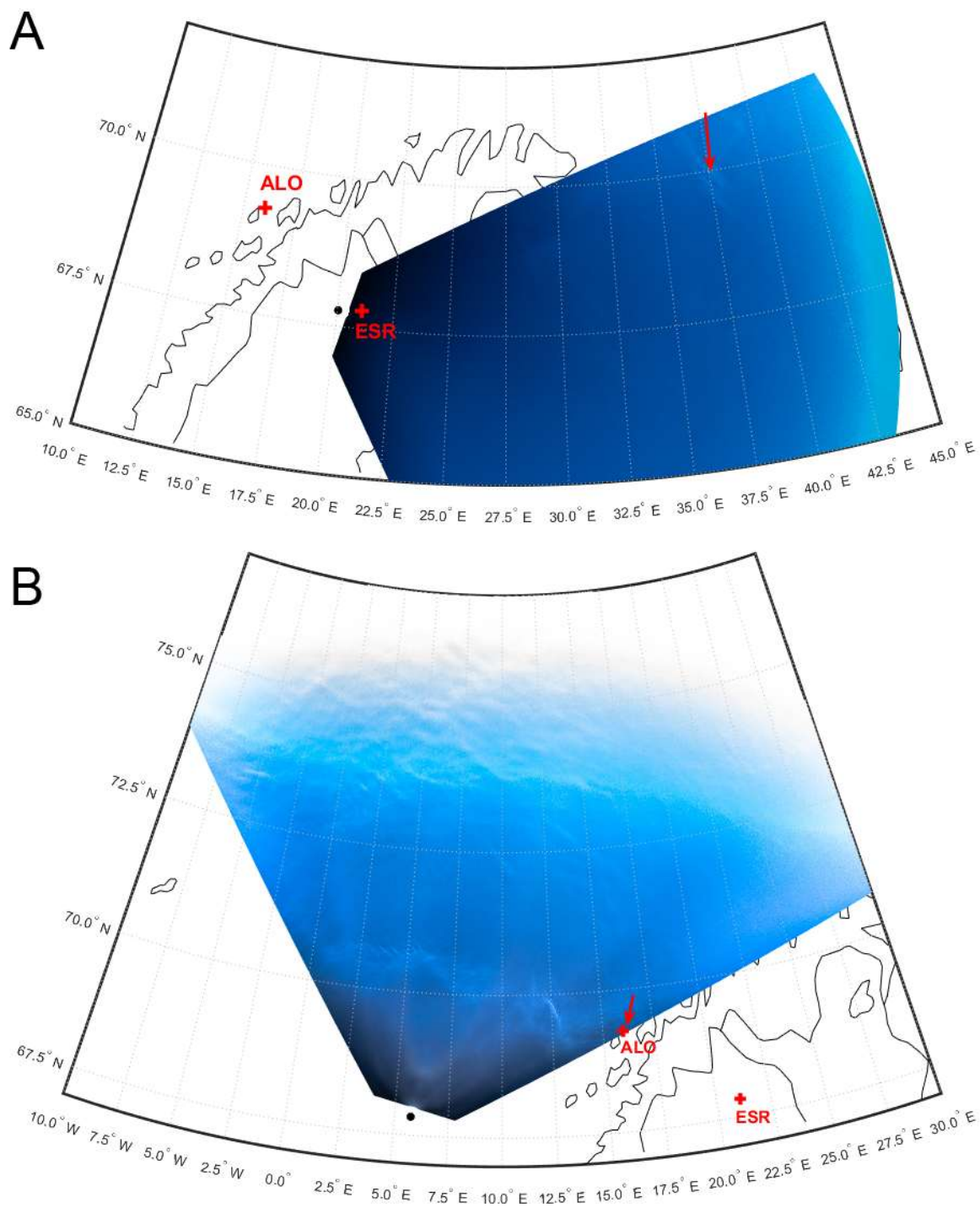
240 simultaneous and common volume (or in proximity) measurements of NLC layers above northern Scandinavia.
241 At Esrange, we use a Rayleigh/Mie/Raman (RMR) backscatter lidar developed by the Bonn University to
242 monitor aerosols in the troposphere, stratosphere and mesosphere as well as to determine temperature profiles in
243 the aerosol-free part of the atmosphere (Blum and Fricke, 2005). The vertical and time resolution of the obtained
244 measurements by the Esrange lidar is 150 m and 4.4 min, respectively. At Andøya, we use an RMR-lidar which
245 has been operated as part of the Arctic Lidar Observatory for Middle Atmosphere Research (ALOMAR). Using
246 measurements of the ALOMAR lidar one can study temperatures and winds in the middle atmosphere, aerosol
247 layers in the stratosphere, polar stratospheric clouds in the lower stratosphere in winter and noctilucent clouds in
248 the mesopause region in summer (Baumgarten, 2010). We use lidars backscattered signals from the 532-nm
249 wavelength channel to measure NLC over Esrange and Andøya during the TRANSAT flight over northern
250 Scandinavia. The vertical and time resolution of the obtained measurements by the ALOMAR lidar is 40 m and
251 30 s, respectively.

252 The results of the lidar measurements during the initial phase of the TRANSAT flight are shown in Fig. 6.
253 The NLC layer is seen in both lidar measurements between 81 and 86 km altitude from 20:30 UTC on 22 June
254 until 01:00 UTC on 23 June. Figure 6b shows raw Esrange lidar counts and Fig. 6c represents the filtered lidar
255 data in the following way. All Esrange lidar data were averaged over a 600 m altitude interval and a 9-minute
256 time interval. Then the atmospheric background was estimated as the average value, and its standard deviation,
257 of the lidar raw counts between 80 and 87 km for each time-averaged measurement. Counts exceeding 1.5
258 standard deviations from the average value were then selected. Figure 6c highlights the main features of the NLC
259 layer seen in Fig. 6b. Between 20 and 22 UTC, the NLC layer lifted up from 84 to 86 km, then it sank to about
260 82 km between 22 UTC on 22 June and 01 UTC on 23 June as demonstrated by both lidars. After 01 UTC,
261 Esrange lidar measurements become too noisy to distinguish the NLC signal from noise. Note that the
262 ALOMAR lidar registered a double-layer NLC structure between 00 and 01 UTC. Another double-layer NLC
263 structure will be discussed in section 4. These height variations of the NLC layer are due to propagating
264 atmospheric gravity waves. Note that it is a very rare case of conducting simultaneous lidar measurements **of**
265 **NLC layers** at Andøya and Esrange (separated by ~250 km) on both sides of the Scandinavian range. **;**
266 **registering about the same NLC layer**. The ALOMAR lidar operated until 12 UTC on 23 June, continuously
267 registering the enhanced NLC layer until about 09:30 UTC, with height variations between 81 and 84 km. The
268 extended NLC field was registered by the SONC imager above northern Scandinavia (not shown in figure)
269 starting from ~22 UTC on 22 June 2024 and during the lidar measurements, thus continuously observing **nearly**
270 the **same** NLC layer from the ground and stratosphere from evening hours on 22 June until morning hours on 23
271 June. **Note that the comparison of the lidars measurements shown in Fig. 6 is qualitative because panels A**
272 **and B are not shown in the same physical units.**



273
 274 **Figure 6: Lidar measurements at Andøya, Norway (A) and Esrange, Sweden (B) during the initial phase**
 275 **of the TRANSAT balloon flight on 22-23 June 2024. (C) Filtered Esrange lidar data averaged over a 600**
 276 **m altitude interval and a 9-minute time interval (see the text).**

277
 278 Figure 7 illustrates the SONC images at 22:04:38 UTC on 22 June and at 09:34:32 UTC on 23 June, i.e., at
 279 the beginning and end of the NLC observations by the Esrange and ALOMAR lidars. At the beginning of the
 280 lidars measurements the NLC observed by the SONC imager were located to the east of the lidars, but at the
 281 same latitude range (Fig. 7a). Later, the SONC imager slowly rotated in the antisolar direction, observing the
 282 east-south-west sector of the sky, and, thus, observations of NLC in the mesopause over the lidars were
 283 impossible. At the same time, at the very end of the ALOMAR lidar observations at about 09:30 UTC on 23
 284 June, the SONC imager looked north-northeast and detected faint NLC at the very edge of the image frame
 285 directly over the ALOMAR lidar (Fig. 7b). At that time, NLC were between 81.6 and 82.0 km (Fig. 6a). Thus,
 286 lidar measurements **can** complement balloon-borne observations, providing information on vertical dynamics of
 287 the NLC layer observed from the stratosphere.



288
 289 **Figure 7: Projection of two SONC images on the Earth's surface at 22:04:38 UTC on 22 June 2024 (A)**
 290 **and at 09:34:32 UTC on 23 June 2024 (B) during the TRANSAT balloon flight. The black dot denotes the**
 291 **balloon position. The red crosses are the position of the ALOMAR (ALO) and Esrange (ESR) lidars. The**
 292 **red arrows show the locations of NLC.**

293

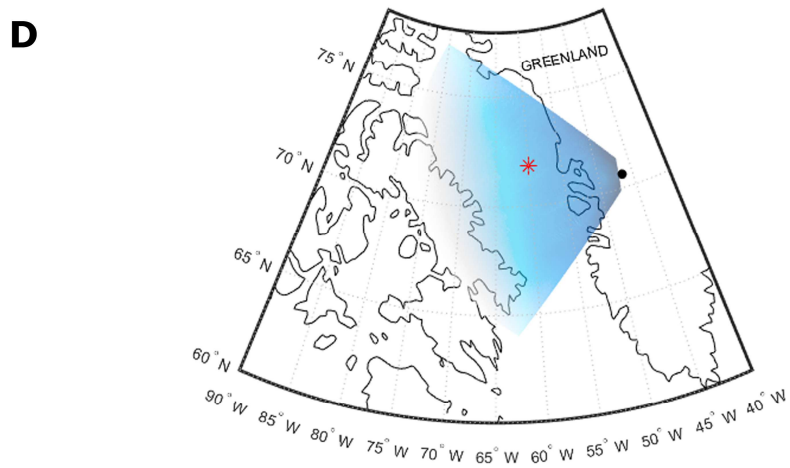
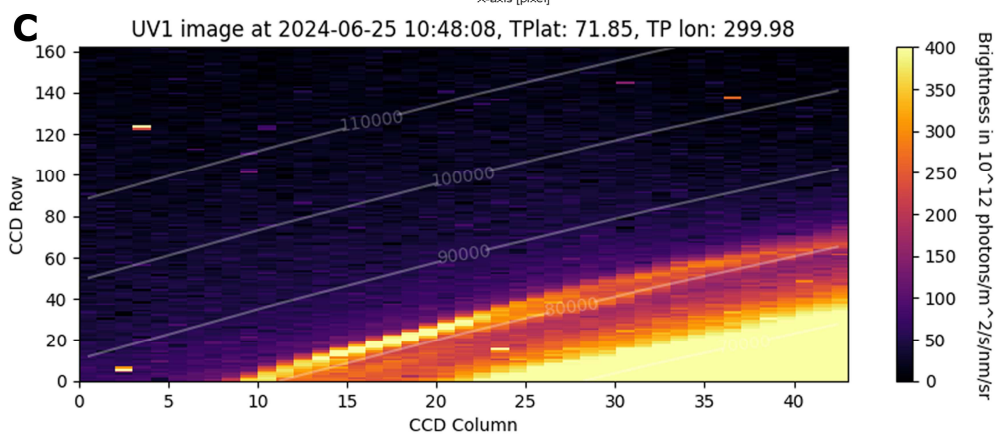
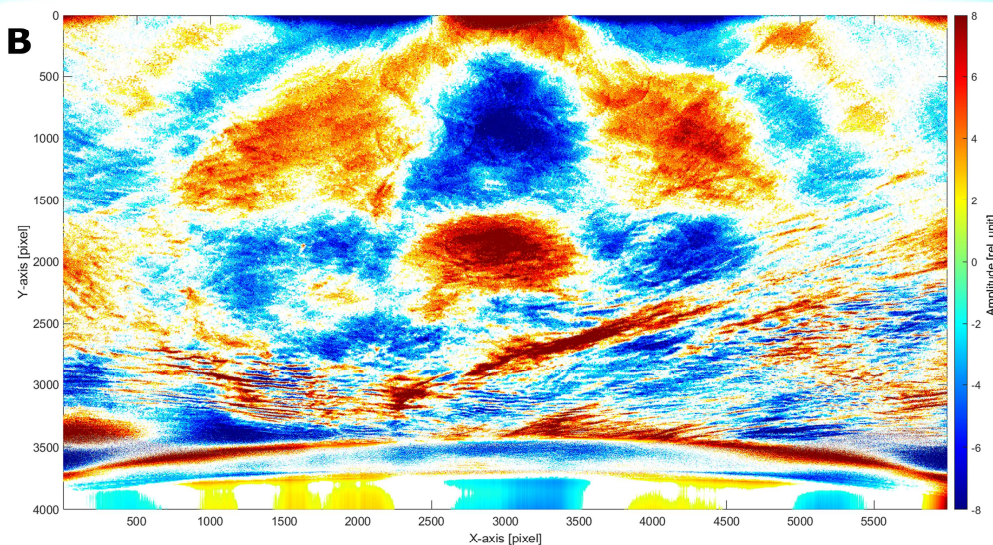
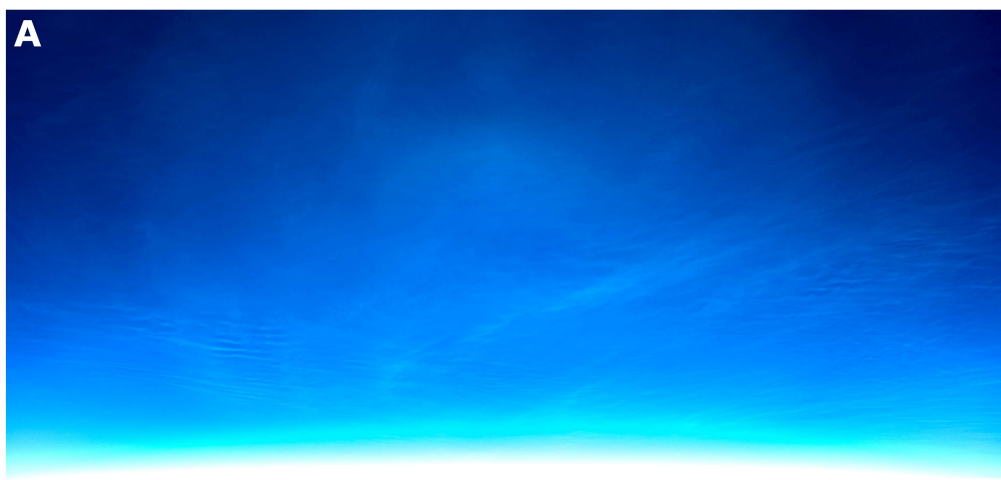
294

3.2 Space measurements

295 During the TRANSAT flight, measurements of PMC from space were also conducted with the MATS
296 satellite. MATS (Mesospheric Airglow/Aerosol Tomography and Spectroscopy) is a Swedish satellite mission,
297 launched in November 2022, designed to investigate polar mesospheric clouds, temperature regime and
298 atmospheric gravity waves in the mesosphere (Gumbel et al., 2020). The MATS satellite utilizes airglow
299 emissions coming from excited molecular oxygen in the near infrared range of the spectrum (760-780 nm, the O₂
300 (0-0) A-band) as well as scattered light from PMC in the ultraviolet (270 and 340 nm). The primary scientific
301 instrument on-board the satellite is the limb imager, a telescope with six wavelength channels that continuously
302 captures images of the atmospheric limb with a field of view of about 40 km in the vertical and 250 km across
303 track at the tangent point. The horizontal and vertical resolution of MATS limb images is 5.7 km and 290 m,
304 respectively. The horizontal resolution is consistent with AIM/CIPS images (Randall et al., 2017) and the
305 vertical resolution of 290 m should be considered high for satellite missions. Using a tomographic analysis of
306 acquired MATS images, one can reconstruct waves in three dimensions and provide 3-dimensional fields of
307 airglow, PMC properties and temperature (Megner et al., 2025).

308 Figure 8 demonstrates an example of MATS images in the UV channel 1 at 270 nm taken at 10:48:08 UTC
309 on 25 June 2024. This measurement was done at the tangent point in the mesopause close to the west coast of
310 Greenland as illustrated in Fig. 8d. One can clearly see the presence of the PMC layer in Fig. 8c as the bright
311 yellow band on the atmospheric limb between 80 and 85 km tangent altitude. The time and location of the PMC
312 by MATS agree very well (time difference of 6 seconds) with the NLC observation obtained from the
313 TRANSAT balloon, with the MATS tangent point being in the field of view of the SONC imager as seen in Fig.
314 8d. Such simultaneous common-volume observation of NLC from the stratosphere and space was made for the
315 second time; the first one was made by the PMC Turbo stratospheric flight and the AIM satellite in July 2018
316 (Fritts et al., 2019). But in the present study this was done for the first time when such a large-scale NLC/PMC
317 field (extending at least 1500 km from north to south) was seen from the stratosphere and from space based on
318 the limb-viewing observation using the MATS satellite. Note that MATS also detected NLC in the next orbit
319 over Greenland and in field of view of the SONC imager at 12:22:16 UTC on June 23 (not shown in figure). In
320 the present study, we do not aim to completely compare all possible NLC observations from the stratosphere and
321 the MATS satellite, but to demonstrate the fundamental possibility of such observations in one figure only. Thus,
322 MATS observed an extended PMC layer in a large volume of the mesopause at least over Greenland, Baffin Bay
323 and Baffin Island. Part of this large-scale NLC field was registered from the stratosphere by the SONC imager
324 shown in Fig. 8a. Figure 8b demonstrates a 2D-filtered image with a second-order polynomial removed from the
325 original image (see section 2.3), which shows NLC modulations due to gravity waves of various scales
326 throughout the lower part of the image. At the same time, images taken from the stratosphere have much higher
327 spatial resolution, showing small- and medium-scale wave dynamics (including smaller gravity waves and
328 turbulent structures) that MATS cannot resolve using the limb-viewing geometry. Thus, studies of spatial-
329 temporal variability of NLC/PMC can be carried out simultaneously from the stratosphere and space,
330 complementing each other.

331



333 **Figure 8: Example of NLC measurements obtained from the stratosphere and space on 25 June 2024**
 334 **during the TRANSAT balloon flight. (A) Image, taken by the SONC imager at 10:48:02 UTC, shows the**
 335 **extended NLC field covering almost the whole image area. (B) 2D-filtered image with a second-order**
 336 **polynomial removed from the original image shown in A (see the text). (C) Image, taken by the MATS**
 337 **satellite at 10:48:08 UTC, illustrate part of the atmospheric limb, with the bright yellow PMC layer seen**
 338 **between 80 and 85 km. Data are shown for the UV channel 1 at 270 nm. (D) Projection of the NLC image**
 339 **shown on Panel A onto the Earth's surface. The black dot is the position of the TRANSAT balloon, the**
 340 **red asterisk marks the MATS tangent point which is in the field of view of the SONC imager.**

341

342 4 Results and Discussion

343 4.1 Nearly continuous observations of NLC

344 The first **unexpected** scientific result is the nearly continuous presence of mesospheric clouds in the
 345 observed latitude range of 60–75°N during 3.8 days of the TRANSAT balloon flight. In total, there were four
 346 intervals of NLC disappearances as shown by the blue circles in Fig. 2a and by the red arrows in Fig. 5. These
 347 events occurred on 23 June at 09:30–10:50 UTC on 23 June, at 18:20–21:20 UTC on 24 June, at 17:45–02:40
 348 UTC on 25-26 June, and at 09:00–11:00 UTC on 26 June. Outside these intervals, NLC were continuously
 349 observed, often with varying brightness and wave modulation.

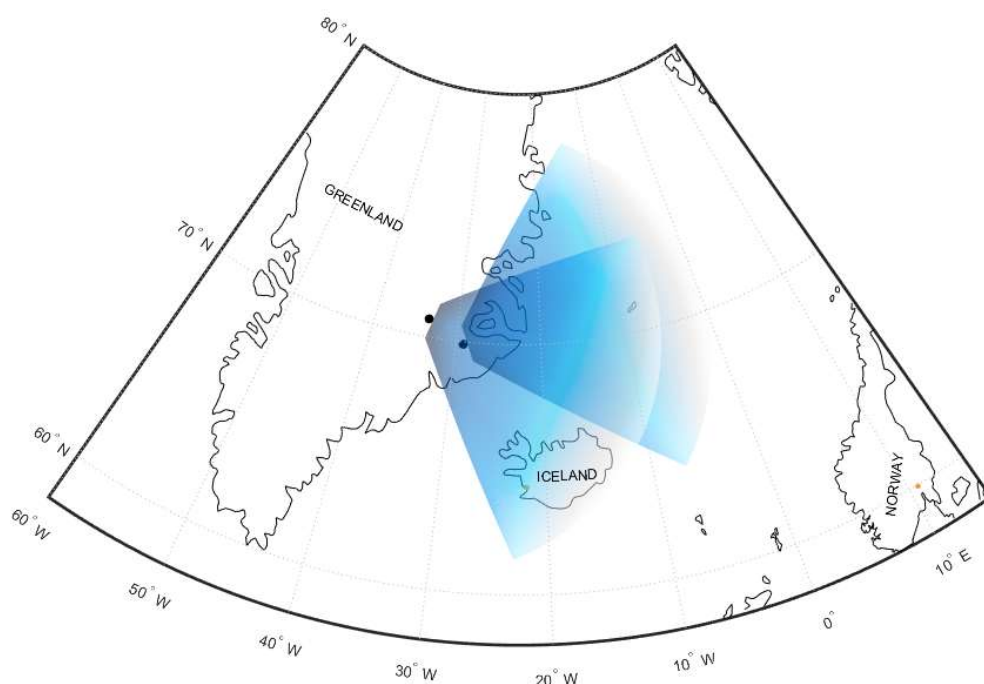
350 These NLC disappearances are not related to local solar time (see four local solar time intervals on the x-axis
 351 in Fig. 5). That is, these NLC interruptions were of a rather spontaneous nature and were not related to solar
 352 thermal tides, which are regular atmospheric variations. Indeed, Fritts et al. (2019) demonstrated more or less
 353 regular NLC disappearances in the evening (18-24 LST) and morning hours (6-12 LST), observed during the
 354 PMC Turbo balloon flight from Sweden to Canada in July 2018. The authors associated this with solar
 355 semidiurnal and diurnal thermal tides in the polar summer mesopause, the amplitudes of which reach 10-20 K,
 356 which is comparable to ones by gravity waves in the mesopause region (Rapp et al., 2002). It should be noted
 357 that this result was obtained on the basis of lidar measurements on the PMC Turbo balloon, that is, obtained with
 358 a very small field of view of a few meters in the mesopause. Therefore, for such a small volume of the
 359 mesopause one can expect the dominant influence of large-scale waves such as solar tides. Note that continuous
 360 lidar observations at 69°N demonstrate strong NLC diurnal variations due to solar tides, with a maximum
 361 occurrence frequency of about 65% in the morning hours and a minimum of about 35% around noon (Fiedler et
 362 al., 2011). In the case of the TRANSAT balloon flight NLC observations were carried out on large scales of
 363 about 1000-1500 km at a time. At such large scales, not only solar tides manifest themselves but also
 364 propagating gravity waves of various scales from 1 to 1000 km. Indeed, a typical picture seen from the
 365 stratosphere was that we saw a disappearance of NLC in one area of the mesopause (for example, in the eastern
 366 part), but simultaneous appearance of other NLC in another part of the mesopause (for example, in the western
 367 part). In other words, large-scale NLC fields were generally represented by numerous wavy patterns of sporadic
 368 nature. One can assume that gravity waves, continuously coming from the lower atmosphere, form a new NLC
 369 and/or modulate an existing NLC layer in different parts of the mesopause (as observed in the present
 370 experiment), thereby dominating solar thermal tides on large scales. At the same time, we should note that this
 371 result was obtained on the basis of a single 3.8-day flight and a limited range of latitudes (60-75°N) and

372 longitudes (45°E-95°W). That is why the present case study cannot claim to be a general statement about the
 373 relative importance of solar tides compared to gravity waves.

374

375 4.2 A case study of the NLC disappearance

376 The second result is connected to the disappearance of NLC at 18:20-21:20 UTC (16:23-19:06 LST) on 24
 377 June 2024 (Fig. 5). This NLC disappearance was observed over the Atlantic Ocean near the east coast of
 378 Greenland and over Iceland as demonstrated in Fig. 9.



379
 380 **Figure 9: Projection of the field of view of the SONC camera on the Earth's surface at 18:20 UTC (16:23**
 381 **LST) and 21:20 UTC (19:06 LST) on 24 June 2024, when no NLC were observed from the stratosphere.**
 382 **The black dots mark the position of the TRANSAT balloon.**

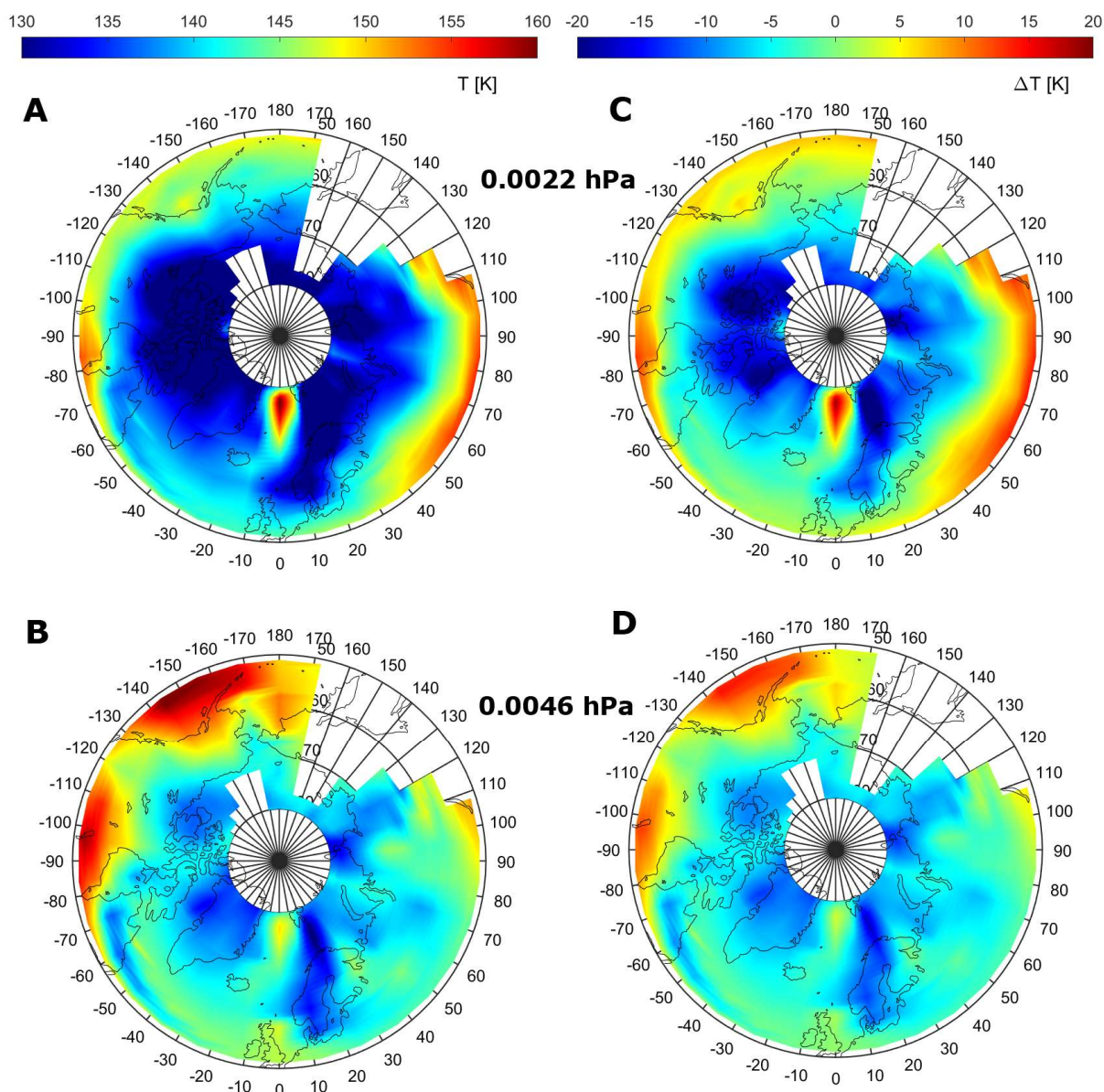
383

384 We have tried to find out the reason for this NLC disappearance. For this data of the Aura/MLS temperature
 385 and water vapor measurements have been used to obtain a comprehensive picture of the mesopause environment
 386 in the region of interest. Aura/MLS temperature and water vapor measurements of ver.5.0 and level 2 data
 387 quality were obtained from the NASA public web-site:

388 https://acdisc.gesdisc.eosdis.nasa.gov/data/Aura_MLS_Level2/. According to the Aura/MLS data quality and
 389 description document (version 5.0x level 2 and 3), for Aura/MLS temperature measurements, the vertical
 390 resolution in the mesopause region is 11 km at 0.01 hPa (~80 km) and 12 km at 0.001 hPa (~90 km). The

391 horizontal resolution (along track) is ~250 km at 0.01 hPa and ~280 km at 0.001 hPa. The pressure range
392 recommended for scientific use is from 261 hPa (~10 km) to 0.00046 hPa (~93 km). Typical precisions for
393 individual Aura/MLS temperature profiles at this altitude range are ± 3.4 – 3.6 K. For Aura/MLS water vapor
394 measurements, the vertical resolution is 8.8 km at 0.01 hPa and 10.3 km at 0.002 hPa. The horizontal resolution
395 is ~725 km at 0.01 hPa and ~350 km at 0.002 hPa. The pressure range recommended for scientific use is from
396 316 hPa to 0.001 hPa. Typical precisions for individual Aura/MLS water vapor profiles are 55% at 0.01 hPa and
397 450% at 0.001 hPa. The description on the MLS temperature product and its validation can be found in
398 Froidevaux et al. (2006) and Schwartz et al. (2008). The validation of water vapor data is described in detail by
399 Read et al. (2007) and Lambert et al. (2007). The frost point temperature in the mesopause was calculated using
400 Aura/MLS water vapor data based on thermodynamics of the vapor pressure of ice (Murphy and Koop, 2005).

401 The results are shown in Fig. 10 demonstrating the following peculiar feature. A prominent localized warm
402 area in the mesopause region at the pressure levels of 0.0022 hPa (about 86 km geometrical height) and 0.0046
403 hPa (about 83 km) was present between Greenland and Scandinavia, with temperatures 20-30 K higher than
404 those in the adjacent mesopause regions at 0.0022 hPa. The location of this warm spot coincides well with the
405 position of the mesopause visible from the TRANSAT balloon when no NLC were seen (Fig. 9). The right
406 column in Fig. 10 shows the differences between the actual temperature measurements and the frost point
407 temperature as calculated using Aura/MLS water vapor measurements, with positive temperature differences
408 being as much as 10-15 K in the center of this warm spot. We double-checked all the Aura/MLS data
409 (temperature and water vapor) which show good quality data suitable for scientific analysis and we could not
410 find any error in these data.



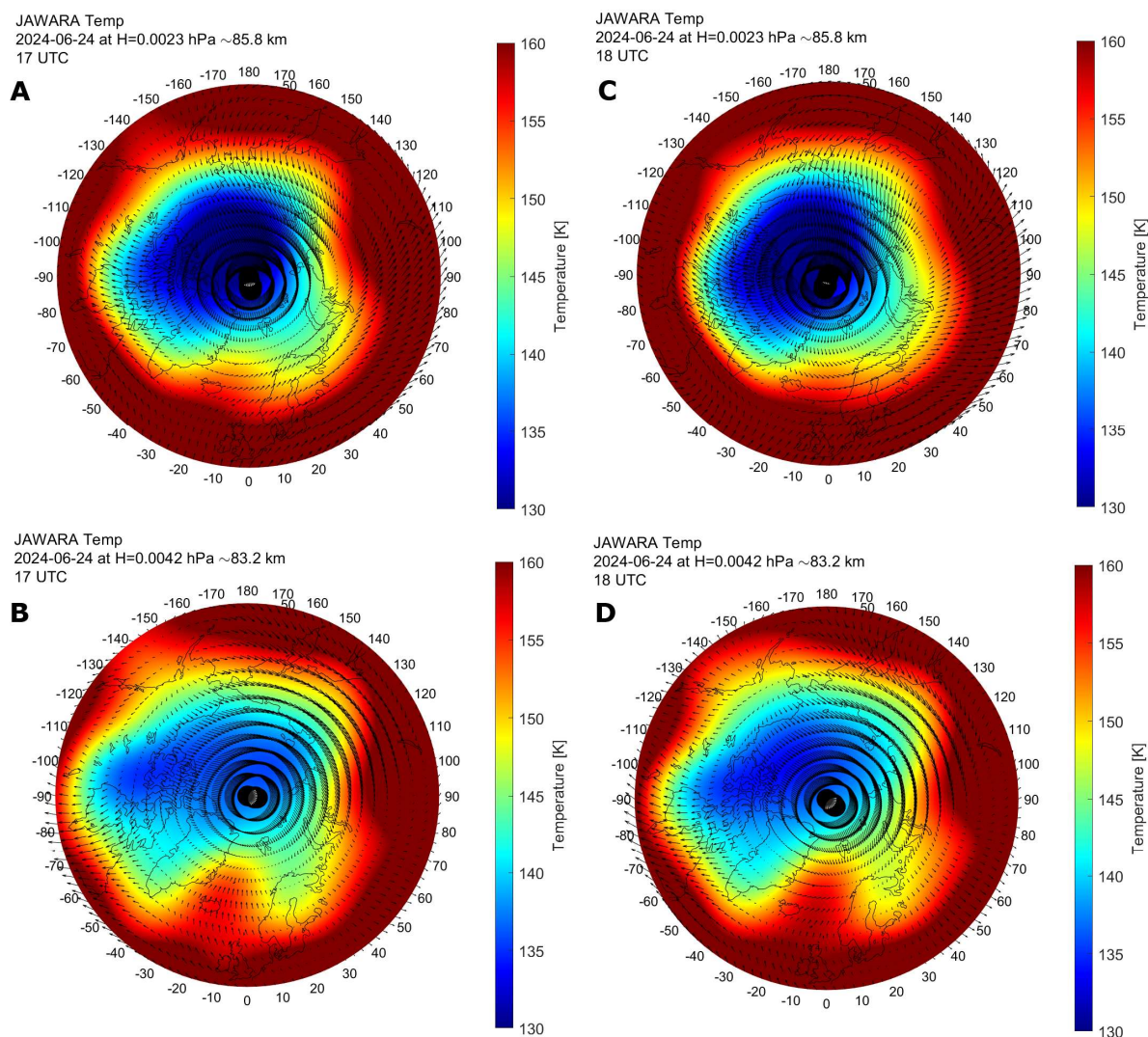
411
 412 **Figure10: (A) Aura/MLS temperature measurements at the pressure level of 0.0022 hPa (~86 km) and (B)**
 413 **at 0.0046 hPa (~83 km) on 24 June 2024. Differences between the temperature and the frost point**
 414 **temperature as estimated based on Aura/MLS water vapor measurements at 0.0022 hPa (C) and 0.0046**
 415 **hPa (D), see the text.**

416
 417 In Fig. 10 (especially in plots for the 0.0046 hPa level), one can note that the warm local region at high
 418 latitudes was an extension of a warm vast area located at mid-latitudes. That is, one can assume that this local
 419 warm region was caused by a jet of warm air mass from middle latitudes to high latitudes. To test this
 420 hypothesis, we apply the Japanese Atmospheric General circulation model for Upper Atmosphere Research Data
 421 Assimilation System (JAGUAR-DAS), which is a data assimilation system for the whole neutral atmosphere
 422 (Koshin et al., 2020; 2022). Specifically, JAGUAR-DAS Whole neutral Atmosphere Reanalysis (JAWARA) has
 423 been considered in the present study. JAWARA is a long-period reanalysis, starting from September 2004,
 424 which covers the altitude range from the surface to the lower thermosphere (~110 km). The vertical resolution of
 425 JAWARA data in the mesopause region between 80 and 90 km is about 0.7 km. JAWARA outputs, distributed

426 on a horizontal grid spacing of 2.81° , include the following hourly data: temperature, zonal, meridional and
 427 vertical wind velocities, geopotential height, temperature tendency due to diabatic heating, zonal and meridional
 428 forcing from the GW parameterization (Koshin et al., 2025). Note that JAWARA assimilates MLS temperature,
 429 meaning that the temperature fields in MLS and JAWARA are not fully independent and the mutual agreement
 430 might be expected because of the data assimilation.

431 JAWARA temperature and neutral wind data in the mesopause region are shown on 24 June 2024 in Fig. 11,
 432 demonstrating the following features. The warm localized spot was present between Greenland and Scandinavia,
 433 and it was most pronounced at 0.0042 hPa, ~ 83 km, (lower plots), which agrees well with the position of the
 434 warm spot represented by Aura/MLS. At the same time, wind velocity vectors show that the local wind jet was
 435 formed, which moved from middle to high latitudes in the region with this warm spot. Thus, this warm spot in
 436 the mesopause was caused by the intrusion of a warm air mass from the middle to high latitudes between
 437 Greenland and Scandinavia. This warm spot induced sublimation of ice particles in the mesopause, which caused
 438 NLC to disappear during the TRANSAT balloon flight over the North Atlantic and the east coast of Greenland in
 439 the evening of 24 June 2024. The mechanism of this air intrusion from middle to high latitudes is beyond the
 440 scope of the present paper.

441



442

443

444 **Figure 11: JAWARA model temperature (color code) and neutral wind velocity vectors (arrows) on 24**
 445 **June 2024. The data are shown at the pressure level of 0.0023 hPa (A and C) and at 0.0042 hPa (B and D),**
 446 **and at 17:00 UTC (A and B) and at 18:00 UTC (C and D).**

447

448 **In general, the relationship between NLC occurrence and ambient mesopause temperature is known.**
 449 **Berger and von Zahn (2002), using model studies with a 3-D general circulation model of the middle**
 450 **atmosphere (COMMA/IAP), demonstrated that the saturation ratio $S=1$ closely coincides with a**
 451 **temperature of 147 K at 83 km altitude at any latitude poleward of 65°N. If the air is supersaturated**
 452 **($S>1$), this condition allows ice particles to exist in the summer mesopause region between 83 and 93 km,**
 453 **depending on latitude. A similar experimental result on the mesopause temperature was found by Dalin et**
 454 **al. (2011), who analyzed Aura/MLS temperatures and NLC occurrences observed from the ground**
 455 **around the globe. The authors found that MLS temperatures around the mesopause control the NLC**
 456 **climatology, i.e., a drop in temperature below the frost point temperature in June corresponds to the**
 457 **beginning of the NLC season, and an increase in temperature above the frost point temperature in August**
 458 **determines the end of the NLC season. The mesopause frost point temperature was estimated to be in the**
 459 **range of 145 to 147 K, with water vapor contents varying between 3.5 and 6.0 ppmv. Hervig et al. (2015),**
 460 **analyzing NLC observations from space using AIM/SOFIE, found that NLC variations are dominated by**
 461 **the mesopause temperature, but a combination of temperature and water vapor content provides the best**
 462 **description of ice water content in the Northern Hemisphere mesopause. At high latitudes, Fiedler et al.**
 463 **(2011) found a strong anticorrelation (-0.96) between LIMA model temperatures and diurnal NLC**
 464 **occurrences above ALOMAR (69°N). At middle latitudes, Gerding et al. (2013) found anticorrelations in**
 465 **the range of $-0.76 \div -0.85$ (depending on altitude) between the NLC occurrence rate and mesopause**
 466 **temperature using lidar measurements at Kühlungsborn (54°N). We should note that the present case**
 467 **study demonstrates not only the well-known link between increased temperature and NLC absence, but**
 468 **more importantly, the intrusion of a warm air mass from the middle to high latitudes in the mesopause**
 469 **region. The latter phenomenon is poorly studied and rarely found in the literature.**

470

471 **4.3 A double-layer structure in NLC**

472 The third early result addresses a double-layer event in NLC observed over Greenland on 25 June 2024. The
 473 reader is recommended to look at the video of NLC image sequence at 05:08-06:49 UTC (02:35-04:08 LST) on
 474 25 June (<https://doi.org/10.7910/DVN/AKJK4P>). One can see at least two NLC layers moving in opposite
 475 directions: one cloud layer visually moved approximately from the top to the bottom of the image frame,
 476 whereas another cloud layer moved in the opposite direction from the bottom to the top. Double-layer and
 477 multiple-layer structures in NLC/PMC have been previously observed and modeled in a number of studies
 478 (Baumgarten et al., 2012; Dubinskii and Popel, 2012; Kaifler et al., 2013; Gao et al., 2017; Li et al., 2017).

479 We have carefully estimated speeds and directions of seven individual NLC points in each of these two
 480 different layers. NLC point trace analysis was applied to the original (unfiltered and unprojected) images. After
 481 completing the trace analysis, the estimation of NLC velocities (speeds and directions) was performed on
 482 projected images. The results of this analysis are as follows. For the NLC layer visually moving from the bottom

483 to the top, the average NLC speed was about 28 m/s, with the average azimuth of about 18° (counting clockwise
 484 from the north). For the NLC layer moving from the top to the bottom, the average NLC speed was about 60
 485 m/s, with the average azimuth of about 193°. These statistical results are summarized in Table 1 as well as
 486 shown in Fig. 12, demonstrating NLC velocity vectors (green and yellow arrows) estimated for the two different
 487 layers. Note that we have taken into account the velocity vector of the TRANSAT flight (zonal and meridional
 488 speed was -10.5 m/s and -7.1 m/s, respectively) when calculating these NLC wind velocities vectors. To
 489 calculate NLC speeds, the average height of the entire cloud layer was chosen as 83 km. Uncertainty in the
 490 height of the NLC layers between 82 and 86 km gives an error of 3-4% of the average NLC speed.

491 It can be assumed that different movements of the two NLC layers were caused by different wind systems
 492 located at different heights in the mesopause region. We cannot measure the heights of the different NLC layers
 493 but we can consider a model simulation to check this assumption. We utilize JAWARA zonal and meridional
 494 wind data in the mesopause region taken at 06:00 UTC on 25 June 2024, i.e., when and where different motions
 495 of the NLC were observed.

496 JAWARA wind data are shown in Fig. 12 by the vector field as well as by the absolute wind speed (color
 497 code). Panel A represents JAWARA wind data at the pressure level of 0.0042 hPa (~ 82.9 km) above Greenland
 498 and seven NLC velocity vectors (green arrows) observed in the NLC layer which was moving in the NNE
 499 direction (visually from the bottom to the top). The average wind speed was about 21 m/s in the direction of 13°
 500 (counting clockwise from the north) in the vicinity of the observed NLC. Panel B illustrates JAWARA wind data
 501 at the pressure level of 0.0017 hPa (~ 86.8 km). One can see about the opposite direction (to SSW) of the model
 502 wind field to that shown on panel A. The average JAWARA wind speed was about 56 m/s, with the average
 503 azimuth of 188°, in the vicinity of the observed NLC. Seven NLC velocity vector are shown by the yellow
 504 arrows which have about the same speed and the direction of motion. All these statistical data are summarized in
 505 Table 1, which demonstrate good agreement between the measured NLC and JAWARA wind velocities both in
 506 the absolute value and in the propagation direction, taking into account their uncertainties. Note that the
 507 JAWARA model has a low horizontal spatial resolution (2.81° or ~ 310 km in latitude and ~ 113 km in longitude
 508 in the analyzed space domain over Greenland) and cannot reproduce wave dynamics due to small-scale gravity
 509 waves. However, in this particular case, the JAWARA model does correspond well to the observed motions of
 510 the two different NLC layers.

511

512 **Table 1.** Statistical parameters of the movement of two different layers observed in NLC during the TRANSAT
 513 balloon flight on 25 June 2024. For comparison, wind data from the JAWARA model are shown. Uncertainties
 514 represent one standard deviation.

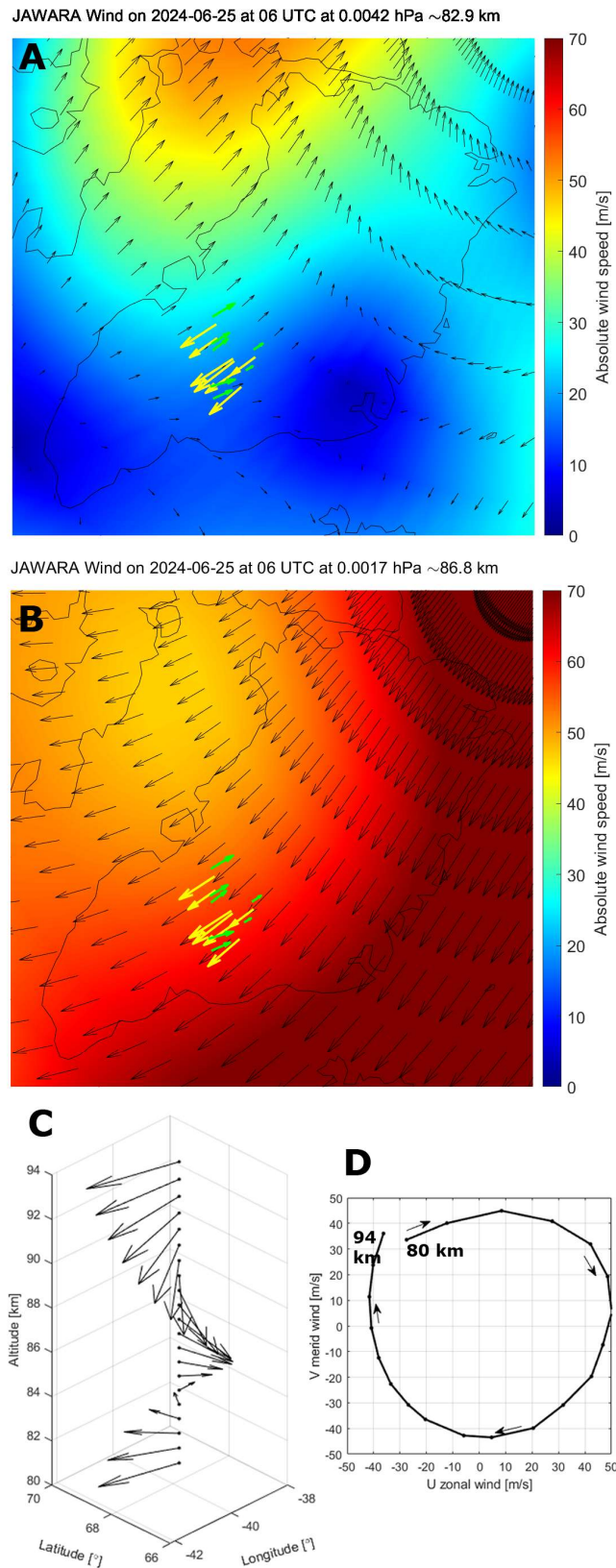
Two NLC layers oppositely moved in image frame	NLC speed (m/s)	NLC azimuth (degree from north)	JAWARA wind speed (m/s)	JAWARA wind azimuth (degree from north)
From bottom to top	27.8 ± 10.0	18.2 ± 8.2	21.0 ± 3.7 at 0.0042 hPa	13.0 ± 12.0 at 0.0042 hPa
From top to bottom	60.5 ± 11.3	192.5 ± 2.2	56.1 ± 2.5 at 0.0017 hPa	188.0 ± 4.3 at 0.0017 hPa

515

516 Panel C of Fig. 12 shows the JAWARA wind velocity vector as a function of altitude for a specific point in
 517 the vicinity of the observed NLC. The cyclic rotation of the wind velocity vector is clearly seen between 80 and

518 94 km altitude, i.e., there was a circular rotation of the wind vector along the azimuth of 360° . Panel D illustrates
519 the corresponding hodograph of the tip of the horizontal wind vector with the subtracted mean velocity values (-
520 33 m/s and -18 m/s for the zonal and meridional wind component, respectively) between 80 and 94 km, that is,
521 perturbations of the horizontal wind velocity. It is well known that a gravity wave induces horizontal wind
522 variations rotating, in general, elliptically with height, and hodograph analysis is commonly used to derive
523 gravity wave parameters (Gossard and Hooke, 1975; Eckermann, 1996 and references therein). In the present
524 case, the hodograph has an almost circular form, implying near circular polarization ($P \approx 0$). Perturbations of the
525 horizontal wind are of 45-50 m/s, and the perturbation vector has a clockwise rotation with increasing height
526 which means that the group velocity of this particular gravity wave was propagating upward (phase velocity was
527 downward). Such an inertia-gravity wave could indeed generate winds in different directions in the given
528 volume of the mesopause, forming a multiple-layer structure from a single NLC layer. The inertia-gravity wave
529 interpretation is a plausible scenario which is consistent with JAWARA winds and NLC motions. At the same
530 time, it should be noted that the background wind in the mesopause region abruptly changes its speed and
531 direction with altitude in summer (Portnyagin and Solovjova, 2000; Conte et al., 2025). Therefore, other
532 mechanisms such as the vertical displacement of the NLC layer by gravity waves, may provide the observed
533 different NLC motions.

534 It is important to note the following. The clockwise wind rotation with altitude by JAWARA was the
535 opposite of that found by Conte et al. (2025), who have analyzed long-term meteor radar measurements in the
536 mesopause region at high latitudes over northern Norway. The authors have obtained the counter-clockwise
537 rotation of the mean wind speed with altitude in the summer time. The same effect of the wind rotation with
538 altitude is predicted by the global empirical wind model for the upper mesosphere/lower thermosphere
539 (Portnyagin and Solovjova, 2000). In this present case, the clockwise rotation of the wind speed indicates the
540 dominance of the inertia-gravity wave over the mean wind rotation speed in the space-time domain under
541 consideration. Also, we should note that even without inertia-gravity waves, winds in the mesopause region can
542 rotate with altitude (Ekman spiral) under the action of the Ekman-type mechanism involving Coriolis force and
543 turbulent viscosity (Chkhetiani and Shalimov, 2010; 2022).



544

545

546

547

548

Figure 12: JAWARA wind data (thin black arrows) at the pressure level of 0.0042 hPa, ~82.9 km (A) and at the pressure level of 0.0017 hPa, ~86.8 km (B) at 06 UTC on 25 June 2024. The color code is the absolute horizontal wind speed. The green and yellow arrows show velocities of NLC moving in opposite directions (see the text). (C) JAWARA wind velocity vector selected for a specific location (68.4°N,

549 39.4°W) as a function of altitude between 80 and 94 km. (D) Hodograph of disturbances of the horizontal
 550 wind velocity vector between 80 and 94 km. The thin arrows show the direction (clockwise rotation) of
 551 wind velocity disturbances with altitude.

552

553 5 Conclusions

554 Observations of noctilucent clouds were performed from the stratosphere during the TRANSAT transatlantic
 555 long-duration balloon flight between Sweden and Canada on 22-26 June 2024. NLC were observed with the
 556 SONC imager composed of three high-resolution SONY α 7 Mark III cameras, stabilized on the TRANSAT
 557 gondola. NLC cannot be detected by an imager from the ground during the midnight Sun season due to strong
 558 background scattering in the lower atmosphere. However, an observation from the stratosphere can detect NLC
 559 during 24 hours. Stratospheric measurements offer **an unprecedented a** view of mesospheric cloud dynamics on
 560 small- and large-scales, bridging the observational gap between ground-based and satellite platforms. The main
 561 results of this study can be summarized as follows:

- 562 1. One wide-angle camera was completely operational during the whole flight for 3.8 days, taking a total of
 563 40,000 images, of which about 6200 images are suitable for scientific analysis.
- 564 2. NLC were detected nearly continuously during the whole flight, showing a strong variability in space and
 565 time. The dominant role of solar thermal tides in the summer mesopause decreases when NLC are observed
 566 on large scales of about 1500 km. At such scales, gravity waves of various scales from 1 to several hundred
 567 km play the largest role, evolving and modulating NLC layers in different regions of the polar mesopause.
 568 Note that this result was obtained on the basis of a single 3.8-day flight and a limited range of latitudes (60-
 569 75°N) and longitudes (45°E-95°W). Thus, the present case study cannot claim to be a general statement
 570 about the relative importance of solar tides compared to gravity waves.
- 571 3. Ground-based support of the TRANSAT balloon campaign was represented by two lidars located at Esrange
 572 and Andoya. Both lidars registered NLC at the time of the initial phase of the balloon flight over northern
 573 Scandinavia. The NLC layered was continuous from 20 UTC on 22 June until 09 UTC on 23 June,
 574 modulated in height between 81 and 86 km, and showing a double-layer structure.
- 575 4. The same mesospheric cloud layer was recorded from the stratosphere and space around noon on 25 June
 576 2024. Such a simultaneous common-volume NLC detection was carried out, for the first time, using a limb-
 577 geometry by the MATS satellite. The extended cloud layer was observed over at least Greenland, Baffin Bay
 578 and Baffin Island, with part of this layer registered from the stratosphere over the west coast of Greenland
 579 and Baffin Bay. Images from the stratosphere showed complex wave dynamics, with interference of small-
 580 scale waves and turbulent regions below what MATS can partly resolve. **Therefore, observations of clouds**
 581 **from the stratosphere and space, using limb geometry, complement each other well.**
- 582 5. Gravity waves had characteristic horizontal wavelengths of 30-40 km for the case study considered in the
 583 mesopause over Greenland on 25 June 2024.
- 584 6. One peculiar case of the NLC disappearance in the polar mesopause in the afternoon of 24 June 2024 has
 585 been analyzed. This cloud disappearance was caused by the localized warm spot in the mesopause region
 586 between Greenland and Scandinavia, as shown by Aura/MLS satellite and JAWARA model data. This warm
 587 spot in the mesopause region was caused by the intrusion of a warm air mass from middle to high latitudes.

588 7. Different movements of NLC were observed in the morning of 25 June 2024 over Greenland. One part of the
589 clouds moved to NNE, another one moved to SSW. A detailed analysis of wind data based on the JAWARA
590 model showed that there were different wind systems between 80 and 94 km altitude over Greenland, with a
591 clockwise wind rotation with altitude. Most likely, a large inertia-gravity wave propagated upwards, causing
592 significant disturbances (45-50 m/s) of the horizontal wind. The wind disturbances caused NLC to move
593 differently at different altitudes. Other mechanisms such as the vertical displacement of the NLC layer by
594 gravity waves may explain the observed different NLC motions.

595 These results demonstrate the scientific value of long-duration stratospheric balloon missions for
596 mesospheric research. Future campaigns of this type will benefit from expanded multi-spectral imaging, real-
597 time data transmission, and coordinated ground-satellite observations to further improve understanding of
598 mesospheric cloud dynamics. A statistical analysis of the wave dynamics observed in NLC during the 2024
599 TRANSAT balloon flight, and investigation of microphysical properties of NLC ice particles will be addressed
600 in future studies.

601

602 **Data availability**

603 Two video files of the SONC experiment are available on the Harvard Dataverse repository
604 (<https://doi.org/10.7910/DVN/AKJK4P>; <https://doi.org/10.7910/DVN/1PHRZU>). Individual NLC images taken
605 from the stratosphere by the SONC experiment that support the findings of this study are available at the
606 HEMERA Data Centre (<https://data.hemera-h2020.eu/atmospheric-balloon-experiments/#/>) as well as will be
607 made available on request.

608

609 **Author contributions**

610 PD, HS, NP, VP, JK and AR have designed two balloon-borne experiments dedicated to studies of noctilucent
611 clouds and infrasound waves. PD wrote the draft of the paper and made analyses of the SONC images, Esrange
612 lidar, Aura/MLS and JAWARA data. LM made analysis of the MATS satellite data. PV and JH performed
613 Esrange lidar measurements. GB performed ALOMAR lidar measurements. DE designed and produced the
614 electric control unit for the SONC imager. All authors discussed the results and contributed to revisions of the
615 text and the figures.

616

617 **Competing interests**

618 The contact author has declared that none of the authors has any competing interests.

619

620 **Acknowledgments**

621 The authors thank the CNES/INSU-CNRS Balloon Programme. The TRANSAT balloon flight was funded and
622 performed by the French Space Agency (CNES) (<https://stratocat.com.ar/fichas-c/2024/KRN-20240622.htm>).
623 The authors thank the Aura/MLS team for providing temperature and water vapor data around the globe during
624 the 2024 TRANSAT balloon flight.

625

626 **Financial support**

627 The SONC imager hardware (imager and electronic control unit) was funded by the Kempe Foundation
 628 (Kempestiftelserna) under grant agreement JCK-1901.4. The infrasound instrument and flight costs of the SONC
 629 and infrasound instruments were financed under research grant 42/17 from the Swedish National Space Agency
 630 (Rymdstyrelsen). The MATS satellite and JH were financed by the Swedish National Space Agency under grant
 631 2021-00052. LM was financed by the Swedish National Space Agency under grant 2022-00108 and the Swedish
 632 Research Council (Vetenskapsrådet) under grant 2021-04876.

633

634 **References**

635 Bailey, S. M., Thomas, G. E., Rusch, D. W., Merkel, A. W., Jeppesen, C., Carstens, J. N., Randall, C. E.,
 636 McClintock, W. E., and Russell, J. M.: Phase functions of polar mesospheric cloud ice as observed by the CIPS
 637 instrument on the AIM satellite, *J. Atmos. Sol.-Terr. Phys.*, 71, 3-4, 373–380.

638 <http://dx.doi.org/10.1016/j.jastp.2008.09.039>, 2009.

639 Baumgarten, G., and Fritts, D. C.: Quantifying Kelvin-Helmholtz instability dynamics observed in
 640 noctilucent clouds: 1. Methods and observations, *J. Geophys. Res. Atmos.*, 119, 9324–9337,
 641 doi:10.1002/2014JD021832, 2014.

642 Baumgarten, G., Chandran, A., Fiedler, J., Hoffmann, P., Kaifler, N., Lumpe, J., Merkel, A., Randall, C. E.,
 643 Rusch, D., and Thomas, G.: On the horizontal and temporal structure of noctilucent clouds as observed by
 644 satellite and lidar at ALOMAR (69N), *Geophys. Res. Lett.*, 39, L01803, doi:10.1029/2011GL049935, 2012.

645 Baumgarten, G.: Doppler Rayleigh/Mie/Raman lidar for wind and temperature measurements in the middle
 646 atmosphere up to 80 km, *Atmos. Meas. Tech.*, 3, 1509-1518. doi:10.5194/amt-3-1509-2010, 2010.

647 Baumgarten, G., Fiedler, J., Fricke, K. H., Gerding, M., Hervig, M., Hoffmann, P., et al.: The noctilucent
 648 cloud (NLC) display during the ECOMA/MASS sounding rocket flights on 3 August 2007: morphology on
 649 global to local scales, *Ann. Geophys.*, 27, 953–965, 2009.

650 **Berger, U., and von Zahn, U.: Icy particles in the summer mesopause region: three-dimensional**
 651 **modeling of their environment and two-dimensional modeling of their transport, *J. Geophys. Res.*, 107,**
 652 **A11, 1366, <https://doi.org/10.1029/2001JA000316>, 2002.**

653 Blum, U., and Fricke, K. H.: The Bonn University lidar at the Esrange: technical description and capabilities
 654 for atmospheric research, *Ann. Geophys.*, 23, 1645–1658, 2005.

655 Chkhetiani, O., and Shalimov, S.: On anomalous wind amplitudes in the lower ionosphere, *J. Atmos. Sol.-*
 656 *Terr. Phys.*, 240, 105960, <https://doi.org/10.1016/j.jastp.2022.105960>, 2022.

657 Chkhetiani, O. G., and Shalimov, S. L.: Helicity in the upper atmosphere and Ekman-type instabilities, *Dokl.*
 658 *Earth Sc.*, 431, 345–350, <https://doi.org/10.1134/S1028334X10030177>, 2010.

659 Conte, J. F., Chau, J. L., Renkowitz, T., Latteck, R., Tsutsumi, M., Jacobi, C., Gulbrandsen, N., and Nozawa,
 660 S.: Observing mesoscale dynamics with multistatic specular meteor radars: first climatology of momentum flux,
 661 horizontal divergence and relative vorticity over northern central Europe, *Ann. Geophys.*, 43, 603–619,
 662 <https://doi.org/10.5194/angeo-43-603-2025>, 2025.

663 Dalin, P., Suzuki, H., Pertsev, N., Perminov, V., Efremov, D., Voelger, P., Narayanan, V. L., Mann, I.,
 664 Häggström, I., Zalcik, M., Ugolnikov, O., Hedin, J., Gumbel, J., Latteck, R., and Baumgarten, G.: Studies of
 665 noctilucent clouds from the stratosphere during the SONC balloon-borne experiment in 2021. *J. Atmos. Sol.-*
 666 *Terr. Phys.*, 240, 105959, doi:10.1016/j.jastp.2022.105959, 2022.

- 667 Dalin, P., Pertsev, N., Perminov, V., Efremov, D., and Romejko, V.: Stratospheric observations of
 668 noctilucent clouds: a new approach in studying middle- and large-scale mesospheric dynamics, *Ann. Geophys.*,
 669 38, 61–71, <https://doi.org/10.5194/angeo-38-61-2020>, 2020.
- 670 Dalin, P., Pertsev, N., Perminov, V., Efremov, D., and Romejko, V.: Looking at “night-shining” clouds from
 671 the stratosphere, *Eos–AGU*, 100, <https://doi.org/10.1029/2019EO118439>, 2019.
- 672 Dalin, P., Pogoreltsev, A., Pertsev, N., Perminov, V., Shevchuk, N., Dubietis, A., Zalcik, M., et al.: Evidence
 673 of the formation of noctilucent clouds due to propagation of an isolated gravity wave caused by a tropospheric
 674 occluded front, *Geophys. Res. Lett.*, 42, 2037–2046, <https://doi.org/10.1002/2014GL062776>, 2015.
- 675 **Dalin, P., Pertsev, N., Dubietis, A., Zalcik, M., Zadorozhny, A., Connors, M., Schofield, I., et al.: A**
 676 **comparison between ground-based observations of noctilucent clouds and Aura satellite data, *J. Atmos.***
 677 ***Sol.-Terr. Phys.*, 73, 14-15, 2097-2109, <https://doi.org/10.1016/j.jastp.2011.01.020>, 2011.**
- 678 Dalin, P., Pertsev, N., Frandsen, S., Hansen, O., Andersen, H., Dubietis, A., and Balciunas, R.: A case study
 679 of the evolution of a Kelvin-Helmholtz wave and turbulence in noctilucent clouds, *J. Atmos. Sol.-Terr. Phys.*,
 680 72, 14-15, 1129-1138, doi:10.1016/j.jastp.2010.06.011, 2010.
- 681 Dalin, P., Pertsev, N., Zadorozhny, A., Connors, M., Schofield, I., Shelton, I., et al.: Ground-based
 682 observations of noctilucent clouds with a northern hemisphere network of automated digital cameras, *J. Atmos.*
 683 *Sol.-Terr. Phys.*, 70, 1460–1472, 2008.
- 684 DeLand, M. T., and Thomas, G. E.: Updated PMC trends derived from SBUV data, *J. Geophys. Res. Atmos.*,
 685 120, 2140-2166, doi:10.1002/2014JD022253, 2015.
- 686 Demissie, T. D., Espy, P. J., Kleinknecht, N. H., Hatlen, M., Kaifler, N., and Baumgarten, G.: Characteristics
 687 and sources of gravity waves observed in noctilucent cloud over Norway, *Atmos. Chem. Phys.*, 14, 12133–
 688 12142, doi:10.5194/acp-14-12133-2014, 2014.
- 689 Dubinskii, A. Yu., and Popel, S. I.: Formation and evolution of dusty plasma structures in the ionosphere,
 690 *JETP Lett.*, 96, 21–26, doi:10.1134/S0021364012130048, 2012.
- 691 Eckermann, S. D.: Hodographic analysis of gravity waves: relationships among Stokes parameters, rotary
 692 spectra and cross-spectral methods, *J. Geophys. Res.*, 101, 19169–19174, 1996.
- 693 Fiedler, J., Baumgarten, G., Berger, U., Hoffmann, P., Kaifler, N., and Lübken, F.-J.: NLC and the
 694 background atmosphere above ALOMAR, *Atmos. Chem. Phys.*, 11, 5701–5717. doi:10.5194/acp-11-5701-2011,
 695 2011.
- 696 Fritts, D. C., Wang, L., Baumgarten, G., Miller, A. D., Geller, M. A., Jones, G., Limon, M., Chapman, D.,
 697 Didier, J., et al.: High-resolution observations and modeling of turbulence sources, structures, and intensities in
 698 the upper mesosphere, *J. Atmos. Sol.-Terr. Phys.*, 162, 57-78, <https://doi.org/10.1016/j.jastp.2016.11.006>, 2017.
- 699 Fritts, D. C., Miller, A. D., Kjellstrand, C. B., Geach, C., Williams, B. P., Kaifler, B., et al.: PMC Turbo:
 700 Studying gravity wave and instability dynamics in the summer mesosphere using polar mesospheric cloud
 701 imaging and profiling from a stratospheric balloon, *J. Geophys. Res. Atmos.*, 124, 6423–6443.
 702 <https://doi.org/10.1029/2019JD030298>, 2019.
- 703 Froidevaux, L., Livesey, N. J., Read, W. G., Jiang, Y. B., Jiménez, C. C., Filipiak, M. J., Schwartz, M. J., et
 704 al.: Early validation analyses of atmospheric profiles from EOS MLS on the Aura satellite, *IEEE Transactions on*
 705 *Geoscience and Remote Sensing*, 44, 5, 1106-1121, 2006.
- 706 Gadsden, M., and Schröder, W.: *Noctilucent Clouds*, Springer, New York, 1989.

- 707 Gao, H., Shepherd, G. G., Tang, Y., Bu, L., and Wang, Z.: Double-layer structure in polar mesospheric
 708 clouds observed from SOFIE/AIM, *Ann. Geophys.*, 35, 295–309, <https://doi.org/10.5194/angeo-35-295-2017>,
 709 2017.
- 710 **Gerding, M., Höffner, J., Hoffmann, P., Kopp, M., and Lübken, F.-J.: Noctilucent cloud variability**
 711 **and mean parameters from 15 years of lidar observations at a mid-latitude site (54°N, 12°E), *J. Geophys.***
 712 ***Res. Atmos.*, 118, 317–328, <https://doi.org/10.1029/2012JD018319>, 2013.**
- 713 Gossard, E. E., and Hooke, W. H.: *Waves in the atmosphere: atmospheric infrasound and gravity waves –*
 714 *their generation and propagation*, Elsevier Scientific Publishing Co, Amsterdam, 1975.
- 715 Gumbel, J., Megner, L., Christensen, O. M., Ivchenko, N., Murtagh, D. P., Chang, S., Dillner, J., Ekebrand, T.,
 716 Giono, G., Hammar, A., Hedin, J., et al.: The MATS satellite mission – gravity wave studies by Mesospheric
 717 Airglow/Aerosol Tomography and Spectroscopy, *Atmos. Chem. Phys.*, 20, 431–455, [https://doi.org/10.5194/acp-](https://doi.org/10.5194/acp-20-431-2020)
 718 [20-431-2020](https://doi.org/10.5194/acp-20-431-2020), 2020.
- 719 Gumbel, J., and Witt, G.: Rocket-borne photometry of NLC particle populations, *Adv. Space Res.*, 28, 7, 1053-
 720 1058, 2001.
- 721 **Hervig, M. E., Siskind, D. E., Bailey, S. M., and Russell III, J. M.: The influence of PMCs on water vapor**
 722 **and drivers behind PMC variability from SOFIE observations, *J. Atmos. Sol.-Terr. Phys.*, 132, 124-134,**
 723 **<https://doi.org/10.1016/j.jastp.2015.07.010>, 2015.**
- 724 Kaifler, N., Baumgarten, G., Klekociuk, A. R., Alexander, S. P., Fiedler, J., and Lübken, F.-J.: Small scale
 725 structures of NLC observed by lidar at 69°N/69°S and their possible relation to gravity waves, *J. Atmos. Sol.-*
 726 *Terr. Phys.*, 104, 244–252, doi:10.1016/j.jastp.2013.01.004, 2013.
- 727 Karlsson, B., and Gumbel, J.: Challenges in the limb retrieval of noctilucent cloud properties from
 728 Odin/OSIRIS, *Adv. Space Res.*, 36, 935-942, doi:10.1016/j.asr.2005.04.074, 2005.
- 729 Koshin, D., Sato, K., Miyazaki, K., and Watanabe, S.: An ensemble Kalman filter data assimilation system
 730 for the whole neutral atmosphere, *Geosci. Model Dev.*, 13, 3145–3177, [https://doi.org/10.5194/gmd-13-3145-](https://doi.org/10.5194/gmd-13-3145-2020)
 731 [2020](https://doi.org/10.5194/gmd-13-3145-2020), 2020.
- 732 Koshin, D., Sato, K., Kohma, M., and Watanabe, S.: An update on the 4D-LETKF data assimilation system
 733 for the whole neutral atmosphere, *Geosci. Model Dev.*, 15, 2293–2307, [https://doi.org/10.5194/gmd-15-2293-](https://doi.org/10.5194/gmd-15-2293-2022)
 734 [2022](https://doi.org/10.5194/gmd-15-2293-2022), 2022.
- 735 Koshin, D., Sato, K., Watanabe, S., et al.: The JAGUAR-DAS whole neutral atmosphere reanalysis:
 736 JAWARA, *Prog. Earth Planet. Sci.*, 12, 1, <https://doi.org/10.1186/s40645-024-00674-3>, 2025.
- 737 Lambert, A., Read, W. G., Livesey, N. J., Santee, M. L., Manney, G. L., Froidevaux, L., Wu, D. L.,
 738 Schwartz, M. J., Pumphrey, H. C., Jimenez, C., Nedoluha, G. E., et al.: Validation of the Aura Microwave Limb
 739 Sounder middle atmosphere water vapor and nitrous oxide measurements, *J. Geophys. Res.*, 112, D24S36, 2007.
- 740 Li, H., Wu, J., and Zhou, Z.: The formation of multiple layers of ice particles in the polar summer mesopause
 741 region, *Ann. Geophys.*, 34, 117–122, doi:10.5194/angeo-34-117-2016, 2016.
- 742 Liu, X., Yue, J., Xu, J., Yuan, W., Russell III, J. M., Hervig, M. E., and Nakamura, T.: Persistent longitudinal
 743 variations in 8 years of CIPS/AIM polar mesospheric clouds, *J. Geophys. Res. Atmos.*, 121, 8390–8409,
 744 doi:10.1002/2015JD024624, 2016.
- 745 Megner, L., Gumbel, J., Christensen, O. M., Linder, B., Murtagh, D., Ivchenko, N., Krasauskas, L., Hedin, J.,
 746 Dillner, J., and Stegman, J.: MATS satellite images (level 1b) of airglow and noctilucent clouds in the

- 747 mesosphere/lower thermosphere, February–May 2023, Dataset version 1.0, Bolin Centre Database,
748 <https://doi.org/10.17043/mats-level-1b-limb-cropd-1.0>, 2025.
- 749 Miller, A. D., Fritts, D. C., Chapman, D., Jones, G., Limon, M., Araujo, D., et al.: Stratospheric imaging of
750 polar mesospheric clouds: a new window on small-scale atmospheric dynamics, *Geophys. Res. Lett.*, 42, 6058–
751 6065, doi:10.1002/2015GL064758, 2015.
- 752 Murphy, D. M., and Koop, T.: Review of the vapour pressures of ice and supercooled water for atmospheric
753 applications, *Q. J. R. Meteorol. Soc.*, 131, 1539–1565. doi:10.1256/qj.04.94, 2005.
- 754 Pautet, P.-D., Stegman, J., Wrasse, C. M., Nielsen, K., Takahashi, H., Taylor, M. J., et al.: Analysis of gravity
755 waves structures visible in noctilucent cloud images, *J. Atmos. Sol.-Terr. Phys.*, 73, 14-15, 2082-2090, doi:
756 10.1016/j.jastp.2010.06.001, 2011.
- 757 Pertsev, N. N., Dalin, P. A., Perminov, V. I., Gusev, N. K., Tsimerinov, E. Yu., Solodovnik, A. A.,
758 Zadorozhny, A. M., Korotyshkin, D. V., and Bordonskiy, G. S.: Analysis of noctilucent cloud fields according to
759 ground-based network and airborne photography data, *Izv. Atmos. Ocean. Phys.*, 60, 2, 187–194,
760 doi.org/10.1134/S0001433824700191, 2024.
- 761 Portnyagin, Y. I. and Solovjova, T. V.: Global empirical wind model for the upper mesosphere/lower
762 thermosphere. I. Prevailing wind, *Ann. Geophys.*, 18, 300–315, <https://doi.org/10.1007/s00585-000-0300-y>,
763 2000.
- 764 Randall, C. E., Carstens, J., France, J. A., Harvey, V. L., Hoffmann, L., Bailey, S. M., Alexander, M.
765 J., Lumpe, J. D., Yue, J. et al.: New AIM/CIPS global observations of gravity waves near 50–55 km, *Geophys.*
766 *Res. Lett.*, 44, 7044–7052, <https://doi.org/10.1002/2017GL073943>, 2017.
- 767 Rapp, M., Lubken, F.-J., Müllemann, A., Thomas, G. E., and Jensen, E. J.: Small-scale temperature
768 variations in the vicinity of NLC: Experimental and model results, *J. Geophys. Res.*, 107, D19, 4392,
769 doi:10.1029/2001JD001241, 2002.
- 770 Read, W. G., Lambert, A., Bacmeister, J., Cofield, R. E., Christensen, L. E., Cuddy, D. T., Daffer, W. H.,
771 Drouin, B. J., Fetzer, E., Froidevaux, et al.: Aura Microwave Limb Sounder upper tropospheric and lower
772 stratospheric H₂O and relative humidity with respect to ice validation, *J. Geophys. Res.*, 112, D24S35, 2007.
- 773 Reimuller, J. D., Thayer, J. P., Baumgarten, G., Chandran, A., Hulley, B., Rusch, D., Nielsen, K., and
774 Lumpe, J.: Synchronized imagery of noctilucent clouds at the day-night terminator using airborne and
775 spaceborne platforms, *J. Atmos. Sol.-Terr. Phys.*, 73, 14-15, 2091-2096, 2011.
- 776 Schwartz, M. J., Lambert, A., Manney, G. L., Read, W. G., Livesey, N. J., Froidevaux, L., Ao, C. O.,
777 Bernath, P. F., Boone, C. D., Cofield, R. E., et al.: Validation of the Aura Microwave Limb Sounder temperature
778 and geopotential height measurements, *J. Geophys. Res.*, 113, D15S11, 2008.
- 779 Suzuki, H., Matsumoto, A., Dalin, P., Nakamura, Y., Ishii, S., Sakanoi, K., Sakaguchi, K., Takada, T., Tsuda,
780 T. T., and Hozumi, Y.: Capability of airline jets as an observation platform for noctilucent clouds at middle
781 latitudes, *Prog. Earth Planet. Sci.*, 9, 11, <https://doi.org/10.1186/s40645-022-00469-4>, 2022.
- 782 Thomas, G.E.: Solar Mesosphere Explorer measurements of polar mesospheric clouds (noctilucent clouds), *J.*
783 *Atmos. Terr. Phys.*, 46, 9, 819-824, 1984.
- 784 Tsuda, T. T., Hozumi, Y., Kawaura, K., Tatsuzawa, K., Ando, Y., Hosokawa, K., et al.: Detection of polar
785 mesospheric clouds utilizing Himawari-8/AHI full-disk images, *Earth Space Sci.*, 9,
786 2021EA002076, <https://doi.org/10.1029/2021EA002076>, 2022.

- 787 Wallis, S., DeLand, M., and Savigny, C.: Did the 2022 Hunga eruption impact the noctilucent cloud season in
788 2023/24 and 2024?, *Atmos. Chem. Phys.*, 25, 3635–3645. <https://doi.org/10.5194/acp-25-3635-2025>, 2025.
- 789 Zadorozhny, A. M., Tyutin, A. A., Witt, G., Wilhelm, N., Wälchli, U., Cho, J. Y. N., and Swartz, W. E.:
790 Electric field measurements in the vicinity of noctilucent clouds and PMSE, *Geophys. Res. Lett.*, 20, 20, 2299-
791 2302, 1993.